Journal of
Marine Science and Engineering

MDPI

Article

Experimental and Numerical Study of the Influence of Clumped Weights on a Scaled Mooring Line

Tomas Lopez-Olocco [1,2,*], Leo M. González-Gutiérrez [1,2], Javier Calderon-Sanchez [1,2], Adolfo Marón Loureiro [3], Leandro Saavedra Ynocente [3], Ana Bezunartea Barrio [3] and Nicolás Vivar Valdés [4]

[1] Universidad Politécnica de Madrid (UPM), 28040 Madrid, Spain; leo.gonzalez@upm.es (L.M.G.-G.); javier.calderon@upm.es (J.C.-S.)
[2] Canal de Ensayos Hidrodinámicos de la ETSI Navales (CEHINAV), Universidad Politécnica de Madrid, 28040 Madrid, Spain
[3] Laboratorio de Dinámica del Buque, Canal de Ensayos Hidrodinámicos el Pardo (INTA-CEHIPAR), 28048 Madrid, Spain; maronla@inta.es (A.M.L.); saavedrayl@inta.es (L.S.Y.); bezunarteaba@inta.es (A.B.B.)
[4] Offshore Engineering Department, SEAPLACE S.L., 28016 Madrid, Spain; n.vivar@alumnos.upm.es
* Correspondence: tomas.lopez@upm.es

Abstract: Recently, several experimental and numerical studies have underlined the advantages of adding clumped weights at discrete positions of mooring lines. To confirm the influence of these weights, an experimental study was performed for a 1:30 scale model of a mooring line. In this study, the clumped weight is modeled as a scaled disc placed at different positions along the mooring line. The series of experiments has been carried out at the CEHIPAR towing tank using a submerged studless chain both with and without clumped weights. The experiments consist of the excitation of the suspension point with horizontal periodic motions using different amplitudes and periods, where the mooring line's tension at the fairlead is measured using a load cell and a dynamometer, and the motion of a part of the line is recorded using low-cost submerged cameras. Similarly to previous experiments, the fairlead tensions increase with higher amplitudes and lower periods, and a clear pattern in the motions of the line at different depths is found. The dissipated energy and the fairlead tension is also increased by the addition of the clumped weight, and the variation of this energy with its position along the line is monitored. The presence of clumped weights is also implemented into a finite element numerical code, previously validated without clumped weights, where all the previous experiments with clumped weights are replicated with remarkable accuracy. This double experimental and computational approach to the problem provides an important dataset for numerical code validations and opens future discussions about the impact of clumped weights on floating platforms.

Keywords: mooring line; clump weights; hybrid mooring system; experiments; floating offshore wind turbines

Citation: Lopez-Olocco, Tomas; González-Gutiérrez, L.M.; Calderon-Sanchez, J.; Marón-Loureiro, A.; Saavedra-Ynocente, L.; Ana Bezunartea-Barrio, A.; Vivar-Valdés, N. Experimental and Numerical Study of the Influence of Clumped Weights on a Scaled Mooring Line. *J. Mar. Sci. Eng.* **2022**, *10*, 676. https://doi.org/10.3390/jmse10050676

Academic Editors: Emre Uzunoglu, Antonio Souto-Iglesias and Carlos Guedes Soares

Received: 30 March 2022
Accepted: 8 May 2022
Published: 16 May 2022

1. Introduction

Floating wind power is considered one of the most promising sources of sustainable energy today. The international framework is clearly favorable for offshore wind as a key technology in meeting decarbonization objectives. The offshore sector is largely being explored due to its higher wind potential when compared to onshore cases. An important factor in motivating offshore locations for wind turbines is the problem that onshore locations are often designated for purposes other than energy production. Classical advantages justify the installation of offshore wind turbines with respect to onshore locations. The energy yield of a wind turbine installed in open sea is, in general, above the production of an onshore location due to higher and steadier winds. The visual and audible impact of a wind farm is less restrictive for the design for offshore than for onshore wind turbines. Finally, most of the world's population is located close to the coastline and transmission losses are therefore low. The growing evolution of offshore wind installations in Europe is quantified in many reports [1], where a tendency toward growth is clearly observed and the important role that it will play in the future is increasingly likely.

The offshore wind energy industry is as economically promising as it is technical challenging, due to the aforementioned *intention to place Floating Offshore Wind Turbines (FOWT) in deeper waters. The reason for this interest is that 61% of US coastal areas, nearly all of Japan's, and various European locations, such as the coast of Norway and Spain and Portugal in the Mediterranean, require floating foundation technology due to the great depth of the water. Today, the majority of European offshore wind turbines are placed in shallow waters, where according to experimental research [2] snap loading may occur more frequently. However, in order to install more offshore farms where better atmospheric conditions are found, highly reliable mooring solutions are required. The mooring system designed for these facilities must be ready to withstand the loads applied by the environment. This imposes the necessity of longer, and therefore heavier and more expensive mooring lines. Due to this necessity, the cost reduction of this growing offshore technology demands the optimization of the mooring line system, where the mechanical fatigue and the extreme and impulsive loads are the most aggressive phenomena for the lines. In order to prevent accidents and long and expensive repairs, a thorough study of the mooring line dynamics is necessary, where extreme loads and fatigue loads are adequately modeled.

We can assert that in the context of offshore wind energy, the reduction of motions allows the turbine to produce power in a wider range of sea states, and lower motions and accelerations reduce the tension of the lines and related costs, see [3]. Therefore, the dual goal is to achieve, when possible, a load reduction of both the mooring lines and the platform motions.

Due to the complex dynamics that govern the mooring line, the presence of snap loads and tension peaks in the mooring lines have been studied in multiple publications, i.e., [4,5]. The evolution of the line tension in such an aggressive and chaotic environment, combined with the fatigue phenomenon and the footprint limitation, makes it necessary to perform a safe and appropriate mooring design in offshore applications. Today, several new concepts and alternative designs for FOWT mooring lines are being studied at water depths greater than 50 m [6]. These modern improvements for mooring systems are to include point masses (Clump Weights) that provide drag and weight to increase the elastic range of the line and enhance the damping of the floating system.

2. State of the Art

The research of mooring systems admits several classifications, being one of them the methodology employed. The most common methodologies are the experimental ones [2,7] that use scaled models, and the numerical one [8,9] where full-scale models are able to be employed. Additionally, there is a vast number of published articles where both approaches are used [10,11]. For each of these methodologies, two types of experiments/simulations have been found in the context of mooring systems, either moored floating objects/structures are placed in a towing tank and are excited by currents or waves [12–20], or isolated mooring lines are forced to move the fairlead with prescribed motion. These last ones can include clumped weights [6,21] or otherwise only the mooring line [2,7–9,11,22–25]. In this experimental and computational study, we follow the second approach and we focus on the isolated mooring dynamics with prescribed motion for the fairlead. The objective of the present study is to extend current research to include the presence of clumped weights, previously addressed by [6] from a quasi-static perspective, but using a dynamic finite element model and comparing its results to the experimental measurements also performed.

The role of the mooring system has a significant contribution to the motion of floating structures, causing about 80% of the total damping of the structure at 200 m depth [26]. This energy dissipation is basically caused by three terms: drag contribution, friction with the seabed, and the internal mechanical damping due to the line deformations. Limiting the scope of research to that found on forced mooring lines, another interesting classification is observable depending on whether the authors are more focused on the damping quantification of the mooring system [26–28] or the mooring dynamics and the different regimes found for different kinds of excitation [10]. The computation of the mooring damping has been computed by quasi-static methods when the mooring line motion is very slow, see [26]. A simple calculation procedure for the practical estimation of damping due to mooring lines is presented and verified experimentally in [29]. The most commonly used method of estimating the total mooring damping is the indicator diagram presented in [28], which has the advantage of including all dynamic responses of the mooring line.

As most of the experiments performed in moored systems are normally scaled models of full-scale prototypes, the importance of the scaling laws and the dimensional analysis of the problem is clear. In [28], one of the first dimensional analyses of the mooring dynamics was performed and, afterwards, the analysis was applied to the scaling of the damped energy. A slightly more simplified dimensional analysis was performed in [25], where the final differential equation that models the phenomenon contains five non-dimensional parameters. It is also worth mentioning that when the experiment must represent a full-scale design, not only should the Froude number associated to gravity remain constant between scales, but also other non-dimensional numbers such as the one associated with line stiffness should be considered. Some experiments [7,30] added a spring at the anchor position to try to keep the stiffness of the line in the proper scaling. One important conclusion of [25] is that even when using a spring connected to the mooring line in order to have a scaled stiffness, a correct scaling is only obtained at quasi-static level. If perfect geometrical and dynamic scaling in vacuum is addressed, the chain must be scaled to have an adequate propagation celerity for longitudinal elastic waves.

Another possible classification comes from the completeness of the differential equation that models the mooring dynamics. In [11], a numerical and experimental study for five different scales of chain mooring systems was performed. They compared the different theoretical approaches to the problem showing the difference to the static case, where no terms including velocities or accelerations were part of the model; the quasi-static case where no terms based on accelerations were considered; and finally, the dynamic approach where accelerations and added mass forces were included.

For the numerical computation of the mooring line, the OPASS [10] code based on the finite element method is used. Other numerical alternatives such as the Open-Moor software, similar to OPASS, is explained in [8] and validated against the forced isolated mooring line described in [25]. An interesting advantage of this latter one is that the time integration is performed using the generalized α-method that permits larger time steps.

Some experiments are able to measure the trajectories and velocities of different points of the mooring line. Different techniques are applied to this process: either image processing methods are applied to snapshots from the camera [2] or sophisticated optical devices such as Qualysis to directly obtain the point position [7]. During the experiments performed in [2] in shallow water, the importance of line stretching for damping was demonstrated also showing that the most critical factors for snap conditions are high pretensions and low amplitudes and periods. A similar study was performed by [22] but also adding a uniform current to the surge and heave fairlead oscillations. A sharp increase of the maximum tension force was observed at large pretension for the mooring line with the surge- and heave-imposed motions.

The dynamic behavior of different mooring lines and the impact of weight and sea bottom friction was analyzed in [7]. An original part of this experimental work is the quantification of the friction coefficients and the effect of the mooring line on the seabed. This work was complemented by the numerical study performed in [9] where an exhaustive sensitivity analysis was performed to evaluate the variability of mooring loads because of inaccuracies in the definition of model inputs.

In [24], the slack-taut regime was searched by numerically changing the initial pretension, amplitude and frequency of the top mooring line excitation were made up of three different parts. The results showed that the slack-taut phenomenon, characterized by maximum tensions several times that of the pretension, would occur beyond a certain threshold of amplitude, frequency, and pretension.

A nonlinear dynamic model of the mooring-line based on FEM simulations was formulated in [23]. An isolated mooring line was tested for a large combination of parameters: pretension, amplitude and frequency, diameter and elasticity modulus. They concluded that the mooring-lines' stiffness presents a hysteresis behavior which becomes more obvious as the suspension point frequency/amplitude gets larger.

We should remark that in this kind of research where an isolated mooring line is studied under forced movement, just a few papers mention the presence of a clumped weight, especially combining the experimental and computational perspectives. Some computational models analyzed implemented the clumped weight as part of the lumped-mass approach, where the total mass of the element (chain and clumped weight) is concentrated in the element's adjacent nodes, see, for example, [18,31]. A numerical-experimental comparison was performed in [21] where a lumped mass computational method was described and compared to the experiments performed in a towing tank. Both approaches were performed using a single clumped weight and limiting the study to a single frequency and amplitude.

The improvement given by the clumped weights was demonstrated in [6] where the key design parameters of clump weights and their effects on mooring system performance were investigated from a quasi-static point of view and assuming that dynamical effects can be neglected. The paper described a methodology of determining the optimum values of these parameters to improve mooring performance.

Table 1 compares the recent research literature of excited mooring lines and the innovation of this study.

As can be observed, most of the papers where the forced mooring lines are studied did not include the clumped weight in the experiment or dynamic numerical simulation. In this paper, we try to fill this gap and analyze experimentally and computationally what effects the presence of a clumped weight has on the mooring line. Another innovation developed for this study is the system designed to track the mooring line kinematics, which is a low-cost system based on an image processing code and submerged cameras. Additionally, the simulation tool OPASS, specifically designed for mooring line dynamics now includes the possibility of clumped weight implementation. Other important conclusions about the evolution of the geometric stiffness of the line and the energy dissipation when clumped weights are included, are also important results obtained from this work.

Table 1. Comparison table of the existing research literature of mooring lines forced oscillations and the present work.

	Methodology	**Results**	**Use of Clumped Weights**
Current work	Experimental and numerical	Dynamic analysis of tension response for different positions of clumped weights, force-displacement curves, PSD analysis, dissipated energy, trajectories, numerical validations with experiments, non-dimensional analysis.	Yes
Nakajima [21]	Experimental and numerical	Fairlead tension time series, frequency response curves of tension. Single frequency and amplitude with clumped weights.	Yes
Luo [6]	Numerical	Dynamic analysis of tension response for different positions of clumped weights.	Yes
Azcona [10]	Experimental and numerical	Fairlead tension, force-displacement curves, trajectories, and numerical validation with experiments.	No

Table 1. *Cont.*

	Methodology	Results	Use of Clumped Weights
Li [23]	Experimental and numerical	Time series of fairlead tension, trajectories, force-displacement curve, dissipated energy, comparison of maximum fairlead tension with the static.	No
Barrera [9]	Experimental and numerical	Experimental fairlead tension time series comparison with numerics, experimental time series of the displacement for different points of the line compared with numerics, sensitivity analysis of the number of elements and computational parameters.	No
Bergdhal [25]	Experimental and numerical	Fairlead tension time series compared with numerics.	No
Yan [27]	Experimental and numerical	force-displacement curve and energy dissipation.	No
Barrera [7]	Experimental	Time series of fairlead tension, fairlead tension-displacement curves, trajectories, accelerations, dissipated energy, sand footprints, hydrodynamic response with different sea states	No
Kitney [30]	Experimental	Force-displacement curves and energy dissipation, non-dimensional analysis.	No
Gao [22]	Experimental	Force-displacement curve, fairlead tension, and PSD analysis, trajectories	No
Hsu [2]	Experimental	Force-displacement curve, energy dissipation and mooring line velocity vectors of image processing.	No
Chen [8]	Numerical	Fairlead tension time series, validation with experiments in the literature.	No
Qiao [24]	Numerical	Fairlead tension time series and PSD analysis, trajectories.	No
Webster [28]	Numerical	Force displacement curves and energy dissipation, non-dimensional analysis.	No

This paper is organized as follows: in Section 3, the case of study, the dimensional analysis, and the experimental setup are presented; in Section 4, the numerical tool used is described and the modeling and implementation of Clumped Weights on it is explained; in Section 5, the experimental results are shown; in Section 6, the numerical and experimental validations are conducted.

3. Experimental Methodology

Among the variety of FOWT designs, the semisubmersible one is receiving particular attention due to various advantages [32]. The two most remarkable ones are: first, these platforms can be fully assembled onshore and deployed to their final operational destination and, second, the mooring systems are widely employed and cost competitive. Recently, different projects have developed proof of concept designs, such as the OC4-DeepCWind shown in Figure 1, in order to generate test data to be used in FOWT modeling tools' validation [33].

Figure 1 shows the OC4-DeepCWind FOWT mooring line arrangement based on three chains separated by 120°. We study a typical deep water configuration where the platform is placed at an approximate sea depth of 200 m.

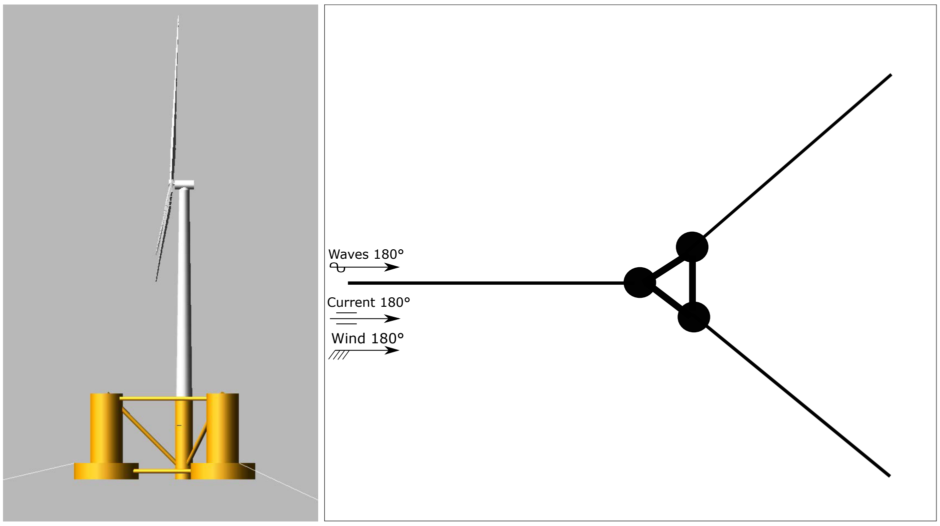

Figure 1. (**Left**) OC4-DeepCWind FOWT design. (**Right**) Top view of the mooring system of the OC4-DeepCWind FOWT [33].

Considering the worst case scenario where waves and wind are aligned in the 180 degree direction as shown in the right panel of Figure 1. This situation, where the wave motion and wind are aligned with the upwind mooring line, provokes the same tension for the two downwind cables, while the upwind line becomes the most loaded one. It is well known, see [26], that in this scenario, surge motions of the moored platform will become very important, and therefore need to be analyzed for the upwind mooring line.

In this paper, three different configurations of mooring line reproducing the upwind mooring line are analyzed: an isolated scaled mooring line and the same line with the addition of a single clumped weight at two different positions. The experiments consist of the excitation of the suspension point, hereafter called fairlead, with horizontal periodic movements reproducing the platform surge motion.

Depending on the installation site, see [10], when surge motion is considered in normal operation conditions, these types of platforms typically have periods ranging from 10 to 30 s and amplitudes from 3 to 12 m.

3.1. Dimensional Analysis

In this subsection, we will try to extend the dimensional analysis performed in [28] to our case where the clumped weight is attached to the mooring line using a line scale factor λ.

Let us start with the analysis of the mooring line equation of motion formulated in global coordinates. This equation will include the elastic deformation of the chain, internal mechanical damping of the chain, and external hydrodynamic forces (weight in water, drag, added mass, and clumped weight). Although the numerical code includes the external action of the sea bottom and structural damping in this dimensional analysis, neither the role of the sea bottom nor the internal damping will be considered. Structural damping is negligible in this kind of mooring dynamics and sea bottom effects are very hard to scale. Similarly to the analysis performed by [25], no bending is considered and we also assume that the experiment is performed in calm water, and therefore, no water current is included in the analysis. When only chains are used as mooring lines, good accuracy is obtained when bending effects are considered negligible, see [10]. The differential equation of motion that supports the dimensional analysis for a mooring line element, is:

$$\gamma \ddot{\mathbf{R}} - \frac{(\partial E A \varepsilon \mathbf{t})}{\partial l_0} - \mathbf{F}_D - \mathbf{F}_W - \mathbf{F}_{CW} - \mathbf{F}_{AM} = 0, \tag{1}$$

where $\mathbf{F}_D$, $\mathbf{F}_W$, $\mathbf{F}_{CW}$, $\mathbf{F}_{AM}$ are the drag, weight in water, clumped weight, and added mass forces to the mooring line, respectively, γ is the mass per unit length of the mooring line, $\ddot{\mathbf{R}}$ is the acceleration of the line element and the partial differential term is the tension of the line element, where ε and $\mathbf{t}$ are the deformation of the line element and the vector tangential to the line element, respectively. Bold text denotes vectorial notation.

The list of dimensional parameters involved in the analysis are:

- F_f Fairlead tension.
- L Total unstretched length of the mooring line.
- H Water depth.
- D Equivalent diameter of the fictitious mooring line that would result if the structural cross-section of the chain were to be formed into a solid, cylindrical rod.
- EA Product of Young's modulus of the chain by the structural cross sectional area of the chain.
- ρ_0 Water density.
- w Chain weight in water per unit volume.
- g Gravity acceleration.
- F_D Mooring line drag force magnitude.
- F_{AM} Mooring line added mass force magnitude.
- ω Fairlead oscillating angular frequency.
- A Fairlead oscillating amplitude.
- F_{DCW} Clumped weight drag force.
- F_{AMCW} Clumped weight added mass force.
- D_{CW} Clumped weight diameter.
- L_{CW} Clumped weight length.
- W_{CW} Weight in water of the clumped weight.
- t Time.

Performing the typical non-dimensional analysis with the previous list of parameters, and using H, D, and D_{CW} as three characteristic lengths corresponding to the water depth, mooring line diameter, and clumped weight diameter, and $\sqrt{H/g}$ and wHD^2/g as characteristic time and mass, respectively. The list of non-dimensional numbers is very similar to the one obtained by [25,28] but adding three new parameters due to the clumped weight's presence. The non-dimensional numbers are classified into three groups according to the situation; they can be summarized as:

Related to the mooring line

- $\Pi_1 = L/H$ Scope of the mooring line.
- $\Pi_2 = \rho_0 g/w$ Ratio between water and line densities.
- $\Pi_3 = F_D/wHD^2$ Drag force coefficient.
- $\Pi_4 = F_{AM}/wHD^2$ Added mass coefficient.
- $\Pi_5 = \omega\sqrt{H/g}$ Ratio between the oscillating frequency and gravitational time.
- $\Pi_6 = A/H$ Ratio between the oscillation amplitude and water depth.
- $\Pi_7 = t\sqrt{g/H}$ Non-dimensional time
- $\Pi_8 = F_f/wHD^2$ Non-dimensional fairlead tension

Related to the mooring line structure

- $\Pi_9 = EA/wHD^2$ Relative stiffness of the mooring line, but also according to [25], the ratio between the propagation celerity of longitudinal elastic waves and the characteristic velocity.

Related to the clumped weight

- $\Pi_{10} = F_{DCW}/wD_{CW}^3$ Clumped weight drag force.
- $\Pi_{11} = F_{AMCW}/wD_{CW}^3$ Clumped weight added mass force.
- $\Pi_{12} = W_{CW}/wD_{CW}^2 L_{CW}$ Weight in water of the clumped weight.

A complete dynamic similarity would imply 12 equal non-dimensional numbers, nine coming from the mooring line plus three from the clumped weight. The first nine non-dimensional numbers include the five used by [25] and are also part of the list of Webster [28] who made a similar analysis but also included three more effects due to bending, water current, and pretension.

In reference [25], it is assumed that two different length scales should be used for the mooring line, one for the water depth λ and another for the mooring line diameter η. Additionally, due to the presence of the clumped weights, two more length scales ψ and α are used. Considering a prototype full-scale size denoted with subindex p and a small-scale model denoted with subindex m, we can express the scaling ratios mathematically as:

$$\frac{L_m}{L_p} = \frac{H_m}{H_p} = \lambda \tag{2}$$

$$\frac{D_m}{D_p} = \eta \tag{3}$$

$$\frac{D_{CWm}}{D_{CWp}} = \psi \tag{4}$$

$$\frac{L_{CWm}}{L_{CWp}} = \alpha \tag{5}$$

We assume first that the water density, ρ_0, the chain density ρ_c, and gravity, g, are the same in the model and prototype. Conserving the non-dimensional numbers Π_5, Π_7, and Π_2:

$$\frac{\omega_p}{\omega_m} = \frac{t_m}{t_p} = \sqrt{\frac{H_m}{H_p}} = \sqrt{\lambda} \tag{6}$$

$$\frac{w_m}{w_p} = 1 \tag{7}$$

Similarly, conserving the non-dimensional numbers Π_3, Π_4, Π_8, Π_9, and Π_6:

$$\frac{F_{fm}}{F_{fp}} = \frac{F_{AMm}}{F_{AMp}} = \frac{F_{Dm}}{F_{Dp}} = \frac{EA_m}{EA_p} = \frac{H_m}{H_p}\frac{D_m^2}{D_p^2} = \lambda\eta^2 \tag{8}$$

$$\frac{A_m}{A_p} = \lambda \tag{9}$$

Finally, conserving the non-dimensional numbers related to the clumped weight Π_{10}, Π_{11}, and Π_{12}:

$$\frac{F_{AMCWm}}{F_{AMCWp}} = \frac{F_{DCWm}}{F_{DCWp}} = \psi^3 \tag{10}$$

$$\frac{(W_{CW})_p}{(W_{CW})_m} = \frac{(D_{CW}^2)_p}{(D_{CW}^2)_m}\frac{(L_{CW})_p}{(L_{CW})_m} = \psi^2\alpha \tag{11}$$

We note that according to Equations (6) and (9), the Froude number defined as $Fr = \frac{A\omega}{\sqrt{gH}}$ is conserved at both scales. Amplitudes and periods of the fairlead motions are scaled according to Equations (6) and (9).

Following the general statements of the dimensional analysis, we should try to scale the maximum number of terms in the differential equations that represent the mooring line. This implies scaling the dominant hydrodynamic loads apart from the weight of the mooring line and the inertial loads. However, as the Reynolds number in the experiments is far from the full-scale value, the hydrodynamic loads due to drag are not scaled according to the scaling laws.

As the OC4-DeepCWind is placed at a 200 m water depth and the CEHIPAR calm water tank has a 6.5 m water depth, a scale factor $\lambda = 1/30$ is chosen. Table 2 summarizes the most important properties of the full-scale mooring system.

Table 2. OC4-DeepCWind mooring system properties [33].

	Value	Units
Number of mooring lines	3	–
Angle between adjacent lines	120	deg
Depth to Anchors below SWL	200	m
Depth to fairlead below SWL	14	m
Radius to Anchors from Platform Centerline	837.6	m
Radius to fairleads from Platform Centerline	40.868	m
Unstretched mooring line length	835.5	m
Mooring line diameter	0.0766	m
Equivalent mooring line mass density	113.35	Kg/m
Equivalent mooring line mass in water	108.63	Kg/m
Equivalent mooring line extensional stiffness	753.6×10^6	N
Hydrodynamic Drag coefficient for mooring lines	1.1	–
Hydrodynamic added-mass coefficient for mooring lines	1.0	–
Seabed drag coefficient for mooring lines	1.0	–
Structural damping of mooring lines	2.0	%

For the scaled experiments, a 27 m long DIN5685A studless chain was selected as its properties are close to the OC4-DeepCWind platform's mooring system when the non-dimensional ratios of $\lambda = 1/30$ and $\eta = 1/23$ are used. The chain used for the dynamic load test is made of stainless steel, see Figure 2 where the main dimensions are indicated. In our case, the diameter D_w of the chain is 7 mm and the length L is 27 m. The length of the link t_w is 16 mm and the diameter of the chain link d_w is 2 mm. The mass per unit length γ of the mooring line is 67.8 g/m.

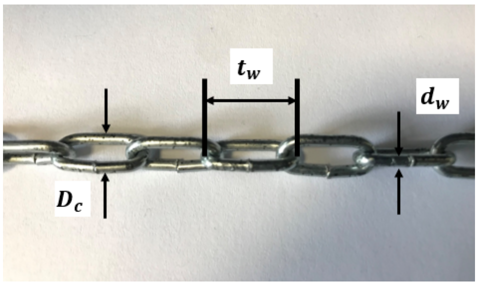

Figure 2. Principal dimensions of the selected chain.

Conserving the non-dimensional number Π_{12} as expressed by Equation (11), the dimensions of the model scale clumped weight are defined as follows. Assuming typical industrial values of a clumped weight, this is a weight in water of 1Tn, we approximate a cylindrical shape volume $V_{CW} = 2.4$ m^3 ($D_{CW} = 1.5$ m, $L_{CW} = 1.33$ m). An example of an industrial clumped weight is shown in Figure 3.

A scale ratio $\psi = 1/18$ is adopted for the clumped weight, not far from the values used to scale the mooring line length ($\lambda = 1/30$) and diameter ($\eta = 1/23$). Instead of using a block shape, in our case, the clumped weight design was modeled as a rigid circular disc characterized by a length L_{CW} and a diameter D_{CW}, in order to maximize drag. To accomplish this, a length scale factor is fixed to the value $\alpha = 1/80$, which is slightly above the other dimensional ratios.

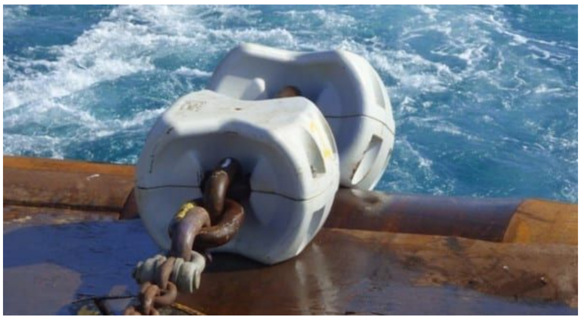

Figure 3. Typical clumped weight used in the offshore industry.

The chosen values for the scaled clumped weight are collected in Table 3 and the manufactured device is shown in Figure 4.

Table 3. Involved variables in the design of the scaled clumped weight.

	Symbol	Value	Units
Mass	$(M_{cw})_m$	122.0	g
Volume of displaced water	$(V_{cw})_m$	80.0	cm^3
Diameter	$(D_{cw})_m$	82.3	mm
Width	$(L_{cw})_m$	16.5	mm

The clumped weight was directly attached to the chain, as shown in Figure 4. The same line has been used for both configurations of the experimental campaign. Consequently, to insert the devices, the chain was cut twice, one for each position of the clumped weight. Special care has been taken to preserve the total length of the line for each configuration. After the aforementioned procedure, the static tension of the line at the fairlead was measured before prescribing the imposed motions.

Figure 4. Designed and manufactured scaled clumped weight (**left**) and snapshot of the clumped weight installed in the mooring line obtained with the submerged camera (**right**).

3.2. Experimental Setup

The experimental campaign was conducted in the calm water tank at the *Canal de Ensayos Hidrodinámicos de el Pardo* (CEHIPAR), see Figure 5a. The main dimensions of the tank were 320 m in length, 12.5 m in width, and water depth is kept at 6.5 m. The tank is equipped with a towing carriage, see Figure 5b, which supports the actuator and the instrumentation for the data acquisition.

(a) (b)

Figure 5. CEHIPAR facilities. (**a**) CEHIPAR towing tank. (**b**) CEHIPAR towing tank carriage.

When the chain is submerged, it acquires a typical catenary shape, see Figure 6. The fairlead is connected to the moving and measurement devices and the bottom end of the chain is anchored to the floor. The anchor consisted of a heavy steel plate, 20 times the weight of the total length of the chain to avoid possible displacements during the tests. Special care has been taken to place the anchor at 25 m in the horizontal direction from the initial fairlead position to have the desired pretension for all the configurations.

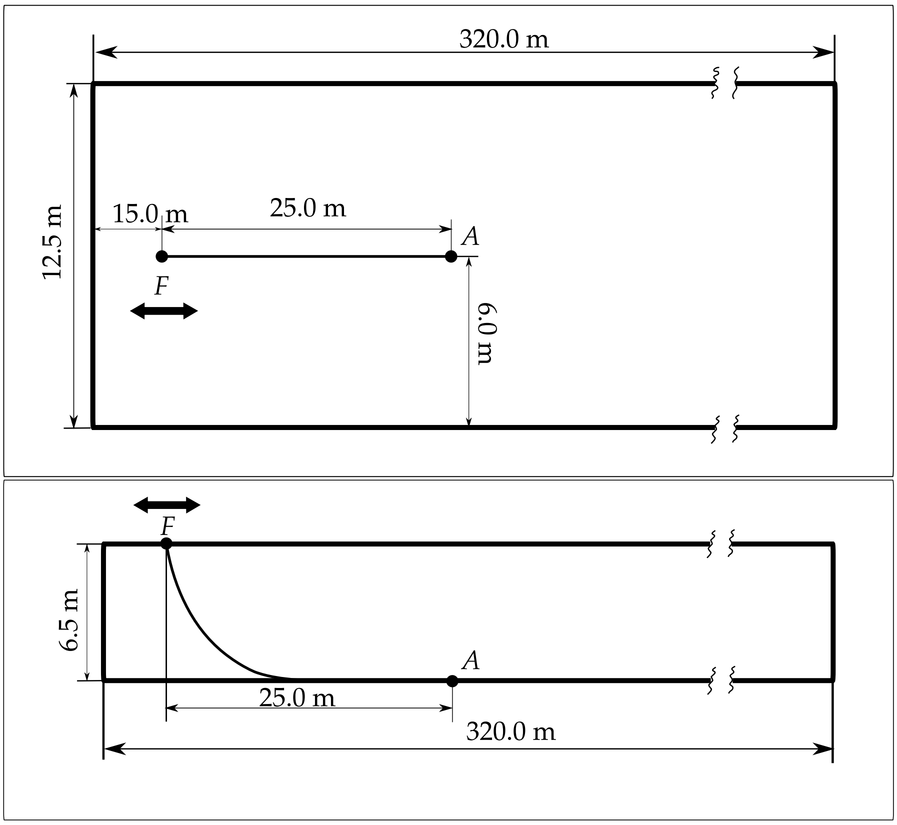

Figure 6. Schematic layout of the top and side views of the experimental setup.

The suspension point was connected to both a load cell and a dynamometer through a metal ring. The measuring devices where fixed to an aluminum beam. Figure 7 shows the described connection. The auxiliary aluminum structure was connected to a linear guide designed to impose surge movements on the water tank when connected to the actuator.

As mentioned, the movement of the suspension point was generated by a mechanical actuator driven by an electrical motor fixed in the structure above the towing carriage shown in Figure 5. The model of the electrical motor is SGMG-44V and its principal technical characteristics are: 4.4 kW of maximum power, 28.4 Nm of maximum torque, and 25 rps of maximum velocity. The maximum acceleration for the motor–actuator system was 1.2 m/s^2, which is higher than the maximum acceleration required in the test matrix for this experimental campaign.

To the measure of the axial tension load of the mooring line, the one-component load cell HBM with an SG full bridge was used. The measured range of the load cell was 0–60 N and the accuracy of the load cell was ± 0.179 N. The sampling rate of the load cell was 100 Hz. The time duration of the force measurement for each case was about 180 s to ensure an acceptable number of cycles in the periodic regime. The connection of the load cell to the beam attached to the actuator allowed the load cell to freely rotate, as can be seen in Figure 7. The load cell used permitted measurement of the tension regardless of the chain rotation. The load cell was covered with a special material to prevent the ingress of humidity into the device during the experiments. The load calibration and determination of uncertainties are described in Appendix A.1.

Figure 7. The load cell and dynamometer connection to the aluminum beam attached to the linear guide.

As it is necessary to simultaneously measure both the horizontal and vertical components of the fairlead tension, a 6 DOF dynamometer was also used. The measured range of the dynamometer was 0–250 N for the x-direction and 0–1000 N for the z-direction. The resolution of the dynamometer was 0.042 N for the x-direction and 0.125 N for the z-direction, and the sampling rate was 100 Hz. To measure the fairlead displacement of the mooring line, a three-component accelerometer HBM with an SG full bridge was used. The measured range of the accelerometer was -2.5 G to 2.5 G and the accuracy of the accelerometer was ± 0.0131 m/s^2, and the sampling rate was 100 Hz. The displacement was obtained by a double numerical integration of the signal using the trapezoid rule. The accelerometer's calibration and determination of uncertainties are described in Appendix A.2.

In this facility, neither the side walls nor the bottom of the water tank are made of transparent material, so a low-cost submerged camera was used to record the mooring movements. An underwater BARLUS camera to record the evolution of the mooring line was used. The technical characteristics were a sampling rate of 24 fps, a 3.6 mm lens, and an image resolution of 5 MP. Special care was taken to place the camera's line of sight perpendicular to the plane of the catenary-shaped line. The camera was fixed to an auxiliary structure to guarantee the same position during the experimental campaign. The distance between the camera and the line was selected to record the largest area possible in order to obtain the best image quality with minimal optical error. A first calibration process, not described here for the sake of brevity, was addressed to determine the equivalent distance of a pixel image.

In order to represent the kinematics of a discrete number of points of the mooring line, equally spaced red marks were distributed along the mooring line. The distance between two adjacent marks along the mooring line is approximately 27 cm and the exact position of these markers is provided in Table 4. The trajectories of the marks were obtained by image processing. This kind of experiments can be found in the literature, see [10] with isolated chains, but are not frequent when clumped weights are added to the line.

Table 4. Position of the red marks used for capturing the line movements.

Marker Number	Position along the Line Measured from the Suspension Point (m)
1	1.62
2	1.89
3	2.16
4	2.43
5	2.70
6	2.97
7	3.24
8	3.51
9	3.78
10	4.05
11	4.32

3.3. Test Matrix

The surge motions of the top of the mooring line are driven by an electrical motor placed on the top of the carriage. The imposed top-end surge motions are sinusoidal motions described by Equation (12).

$$\delta = A \sin \frac{2\pi t}{T}, \tag{12}$$

where δ represents the fairlead horizontal displacement with respect to the position where the pretension is measured, A and T represent the imposed amplitude and period, respectively. The amplitude values used are in the range [0.125,0.225], which correspond to [3.875,6.975] at real scale, and are presented in Table 5. Model-scale and the corresponding full-scale periods are presented in Table 6.

Table 5. Amplitudes of the fairlead motions for $\lambda = 1/30$.

ID	Model Scale (m)	Full Scale (m)
A 1	0.225	6.975
A 2	0.200	6.200
A 3	0.175	5.425
A 4	0.150	4.650
A 5	0.125	3.875

A total number of 105 dynamic tests were conducted for the surge motion, and each test had a duration of 180 s to ensure an acceptable number of cycles. For each amplitude and period, three configurations have been tested: in the first, no clumped weight is used and, in the other two, the clumped weight is placed at $L_s/3$ (Configuration 1) and $L_s/2$ (Configuration 2) from the fairlead, where L_s is the suspended length of the line. Figure 8 shows the catenary-shaped mooring line in the three configurations.

Table 6. Fairlead motions periods in seconds for $\lambda = 1/30$.

ID	Model Scale	Full Scale
T 1	2.80	15.590
T 2	3.00	16.703
T 3	3.50	19.487
T 4	4.00	22.271
T 5	4.50	25.055
T 6	5.00	27.839
T 7	5.50	30.623

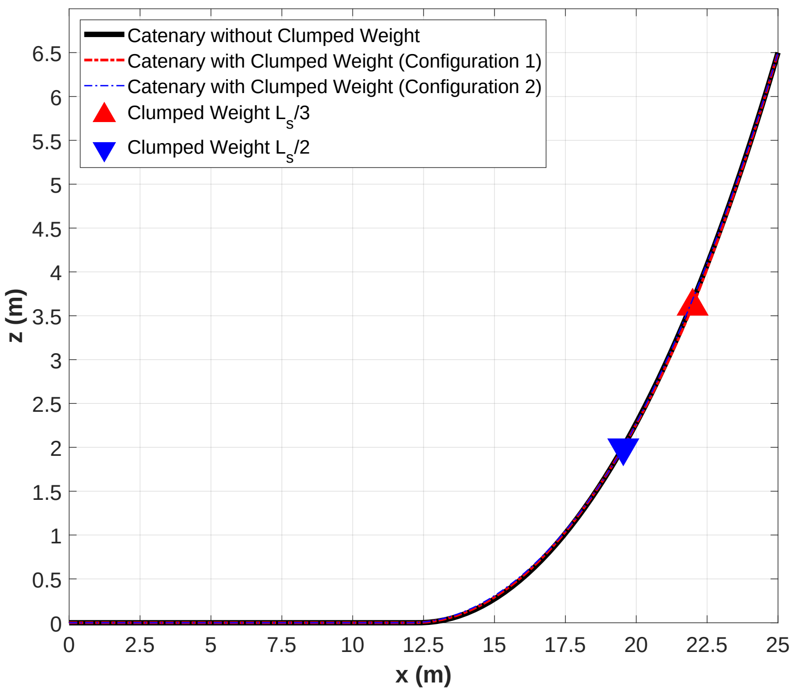

Figure 8. All three tested configurations. Note: the three lines are almost overlapping, the catenary shape is slightly changed in each configuration.

4. Computational Model

4.1. Quasi-Static Modeling

For the quasi-static analysis, the theory developed by [34] is used. The analytical equations for a line, with a portion of the line resting on the seabed, are:

$$x_F - x_A = L - \frac{V_F}{\gamma_w} + \frac{H_F}{\gamma_w} \ln\left[\frac{V_F}{H_F} + \sqrt{1 + \left(\frac{V_F}{H_F}\right)^2}\right] + \frac{H_F L}{EA} + \frac{C_B \gamma_w}{2EA}\left[-\left(L - \frac{V_F}{\gamma_w}\right)^2 + \left(L - \frac{V_F}{\gamma_w} - \frac{H_F}{C_B \gamma_w}\right) MAX\left(L - \frac{V_F}{\gamma_w} - \frac{H_F}{C_B \gamma_w}, 0\right)\right], \tag{13}$$

$$z_F - z_A = \frac{H_F}{\gamma_w}\left[\sqrt{1 + \left(\frac{V_F}{H_F}\right)^2} - 1\right] + \frac{V_F^2}{2EA\gamma_w}, \tag{14}$$

and

$$\gamma_w = \frac{\rho_c - \rho_0}{\rho_c} \gamma g, \tag{15}$$

where L is the total unstretched length of the line, EA is the extensional stiffness, γ_w is the apparent weight in fluid per unit length, C_B is the seabed friction coefficient, H_F and V_F are the horizontal and vertical forces applied at the fairlead, respectively, ρ_c is the density of the chain, ρ_0 is the density of the water, γ apparent mass per unit length of the chain, and g is the acceleration due to gravity.

A scheme of the mooring line where a clumped weight has been added is illustrated in Figure 9. We can divide the line into two segments, the first segment going from the anchor to the position of the point mass, while the second one starts at the point mass location of the fairlead. The equations of the catenary are applied to each segment before and after the clumped weight was added and solved together as a nonlinear system of six equations: four catenary Equations (13), (14), (16) and (17) and two extra equations for the local force equilibrium at the position of the clumped weight. A Newton–Raphson iterative method is used to solve the resulting system of 6 nonlinear equations with 6 unknowns: H_A, V_A, H_F, V_F, T_{Hs2}, T_{Hs1}, T_{Hs1}, T_{Hs2} , T_{Vs1}, T_{Vs2}, x_P, z_P.

$$x_F - x_A = \frac{H_F}{\gamma_w}\left\{\ln\left[\frac{V_F}{H_F} + \sqrt{1+\left(\frac{V_F}{H_F}\right)^2}\right] - \ln\left[\frac{V_F-\gamma_w L}{H_F} + \sqrt{1+\left(\frac{V_F-\gamma_w L}{H_F}\right)^2}\right]\right\} + \frac{H_F L}{EA} \tag{16}$$

$$z_F - z_A = \frac{H_F}{\gamma_w}\left[\sqrt{1+\left(\frac{V_F}{H_F}\right)^2} - \sqrt{1+\left(\frac{V_F-\gamma_w L}{H_F}\right)^2}\right] + \frac{1}{EA}\left(V_F L + \frac{\gamma_w L^2}{2}\right) \tag{17}$$

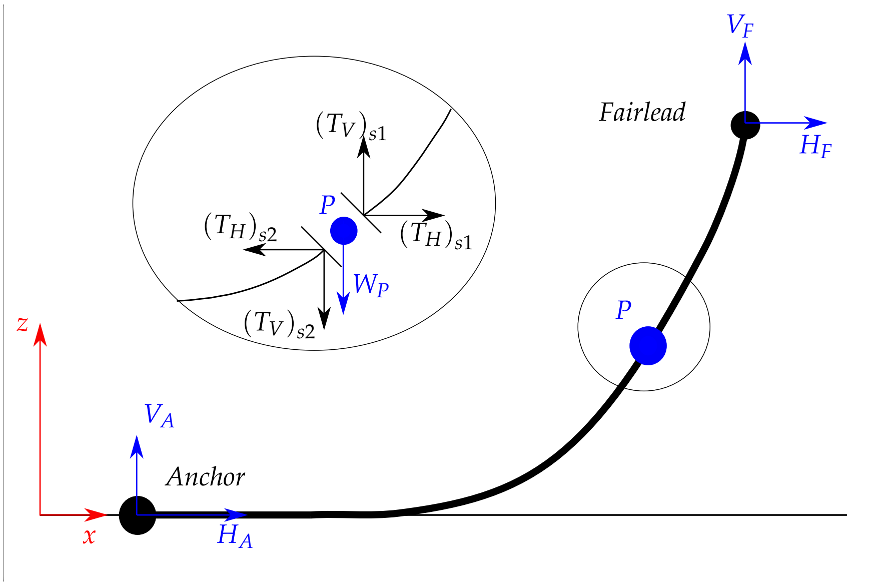

Figure 9. Free body diagram of a mooring line with a clumped weight positioned at point P.

Note that the equations are presented slightly differently than in [34] because of the change in the reference system and the assumption that the chain is modeled as a Morison's slender cylinder.

4.2. Basic Dynamic Equations

Using the finite element method, the partial differential Equation (PDE) (18) which models the mooring line elements is transformed into a nodal system of ordinary differential equations (ODE). This ODE system is discretized in time and solved by the OPASS code [10].

$$\gamma\ddot{\mathbf{R}} + C_4(1+\varepsilon)\left[\ddot{\mathbf{R}} - \left(\ddot{\mathbf{R}}\cdot\mathbf{t}\right)\mathbf{t}\right] - \frac{(\partial EA\varepsilon\mathbf{t})}{\partial l_0} - \frac{(\partial\beta EA\dot{\varepsilon}\mathbf{t})}{\partial l_0} - \mathbf{F_1} - \mathbf{F_2} - \mathbf{F_3} = 0, \tag{18}$$

where γ is the line mass per unit of mooring line unstretched length, $\mathbf{R}$ is the position of the line element analyzed, $\mathbf{t}$ is the vector tangential to the line at the point analyzed, ε is the deformation, EA is the extensional stiffness, C_4 is constant for the calculation of the hydrodynamic inertial force per unit of unstretched line length, β is a coefficient for the calculation of the structural damping force, and l_0 is the location of the point analyzed along the line.

The external forces $\mathbf{F_1}$, $\mathbf{F_2}$, $\mathbf{F_3}$ are the resultant forces from weight in water, the tangential and normal drag components, respectively, per unit of unstretched length. These hydrodynamic forces are model-led by Equations (19)–(21).

$$\mathbf{F_1} = -\gamma_r g \mathbf{k} = -\frac{\rho_c - \rho_0}{\rho_c} \gamma g \mathbf{k}, \tag{19}$$

where $\mathbf{k}$ is the unit vector parallel to the z axis.

The normal and tangential drag forces are modeled by the Morison equation ([35]), as follows:

$$\mathbf{F_2} = \frac{1}{2} C_{dt} D \rho_0 (1+\varepsilon) V_t^2 \mathbf{t} \tag{20}$$

$$\mathbf{F_3} = \frac{1}{2} C_{dn} D \rho_0 (1+\varepsilon) V_n^2 \mathbf{n}, \tag{21}$$

where the vector $\mathbf{V} = V_t \mathbf{t} + V_n \mathbf{n}$ denotes the relative velocity between the water and the mooring line, expressed by its tangential and normal components. Moreover, C_{dt} and C_{dn} are the tangential and normal drag coefficients of the bare line.

Using bar elements for the spatial discretization of the mooring line, linear polynomials for the elements' internal interpolation of the line motions, and 0-order polynomials for the mass and added mass terms, the global equation of motion is condensed into Equation (22)

$$M \cdot \ddot{\mathbf{X}} + C \cdot \dot{\mathbf{X}} + K \cdot \mathbf{X} + \mathbf{F} = 0, \tag{22}$$

where M is the mass matrix of the system, C is the damping matrix, K is the stiffness matrix, $\mathbf{F}$ is the vector of external forces, and $\ddot{\mathbf{X}}$, $\dot{\mathbf{X}}$, and $\mathbf{X}$ are, respectively, the vectors of acceleration, velocities, and positions of the line DOF defined at the nodes.

4.3. Clumped Weight Implementation

The presence of a clumped weight modifies the system of Equation (22), where an additional weight in water, drag, inertia, and added mass due to the clumped weight are added to the matrix system. We assume a rigid union between the clumped weight and the mooring line, where all local forces due to the clumped weight are distributed per unit length. The external forces acting on the mooring line element i are weight in water $\mathbf{F_{1i}}$, tangential drag $\mathbf{F_{2i}}$ and normal drag $\mathbf{F_{3i}}$, and the added mass $\mathbf{F_{4i}}$.

The weight of the mooring line element is increased by the weight of the clump weight, resulting in an external force for that element described in Equation (23), where W_{CW} is the weight of the Clump Weight in water and L_i is the length of the chain element.

$$\mathbf{F_{1i}} = -\left(\gamma_r g + \frac{W_{CW}}{L_i} \right) \mathbf{k} \tag{23}$$

As described in Section 3.1, the shape of the clump weight is a circular disk represented as schematic view in Figure 10.

For those elements that include a clumped weight, the tangential drag is modified according to Equation (24), where the second term is the tangential drag force per unit length added by the clumped weight. The tangential drag coefficient C_{dtCW} is interpolated for every time step according to its local clumped weight Reynolds Number. The selected C_D-Re curve is illustrated in [36].

$$C_2^{CW} = \frac{1}{2} \rho_0 C_{dt} D + \frac{1}{2} \rho_0 C_{dtCW} \frac{\pi D_{CW}^2}{4} \frac{1}{L_i} \tag{24}$$

Regarding the inertial forces, the implementation of the clumped weight impacts the mass matrix. The body mass of the element that includes the clump weight is increased, and the mass per unit length of line γ is augmented by the mass of the device per unit length of the line in a quantity of $\frac{m_{CW}}{L_i}$.

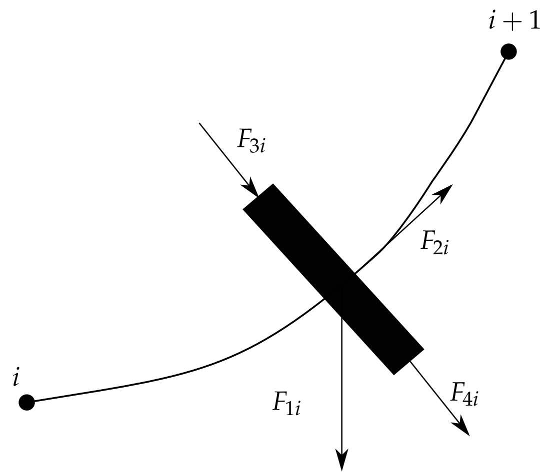

Figure 10. External forces acting on an element of line.

The added mass force per unit of unstretched line length was calculated in OPASS based on a normal added mass coefficient C_{mn} for the Morison approach.

$$C_4^{CW} = C_{mn}\rho_0 \frac{\pi D^2}{4} + \frac{1}{3}\rho_0 \frac{D_{CW}^3}{L_i} \tag{25}$$

The second term of Equation (25) is the well-known theoretical ideal fluid added mass per unit length of the mooring line element for a circular disk described by [37]. This term is only considered for those elements that include a clump weight.

4.4. Computational Parameters Used in the Simulations

The dimensions of the chain where described in Section 3.1. A mass per unit length $\gamma = 0.0678$ Kg/m and a wire diameter of the chain link $d_w = 2$ mm were measured. Equation (26) provided by [38] determines the axial stiffness in kN when d_w is in meters of the chain used in the simulations.

$$EA = 0.854 \cdot 10^8 d_w \tag{26}$$

As the computational model considers the chain to be a line with a constant circular section (Morison approach), an equivalent hydrodynamic diameter has to be determined. Consequently, the diameter of the equivalent circular section was calculated assuming the same mass per unit length of the chain, see Equation (27). This procedure is based on the assumption that in catenary mooring lines, the weight in water has a dominant effect on the motions, loads, and restoring forces.

$$D = \sqrt{\frac{4\gamma}{\pi\rho_c}} \tag{27}$$

The added mass coefficient C_{mn} of 1.0 is determined following the standards of [39] and the normal and tangential drag coefficients C_{dn} and C_{dt} were obtained following the indications of DNV [40]. For a studless chain, this guideline provides a value for C_{dn} of 2.4 and, for C_{dt}, a value of 1.15; these values correspond to the wire diameter of the chain link. For the numerical implementation, the values have to be referred to the equivalent hydrodynamic diameter, and in order to obtain the equivalent drag coefficient, we assume the same drag force per unit length and proceed as follows:

$$C_{Dn} = \frac{C_{dn} d_w}{D} \quad ; \quad C_{Dt} = \frac{C_{tn} d_w}{D} \tag{28}$$

The contact model implemented in OPASS uses bi-linear springs. When a node is in contact with the seabed, a spring with stiffness K_{sc} provides the floor reaction force per indentation depth and per unit of line length. A damping D_{sc} is also included in the model. The resulting parameters are summarized in Table 7.

Table 7. Parameters of the computational model.

	Value	Units
Equivalent hydrodynamic diameter (D)	0.0033	m
Unstretched Length (L)	27.0	m
Line mass density (ρ_c)	7850	Kg/m^3
Mass per unit length (γ)	0.0678	Kg/m
Axial stiffness (EA)	3.416×10^5	N
Coefficient for the structural Rayleigh damping (β)	0.0007	–
Added mass coefficient (C_{mn})	1.0	–
Normal drag coefficient (C_{Dn})	1.445	–
Tangential drag coefficient (C_{Dt})	0.697	–
Vertical seabed stiffness (K_{sc})	20.0	N/m^2
Vertical seabed damping (D_{sc})	0.1	Ns/m^2
Tangential friction coefficient (C_{ft})	0.0	–
Normal friction coefficient (C_{fn})	0.0	–

5. Experimental Results

Once the shape and position of the catenary have been verified, the static tension measured by the load cell is compared to the theoretical pretension predicted with the formulation described in Section 4.1 as a function of the offset value, see Figure 11. We define the offset distance as the horizontal distance between the top end of the mooring line and the anchor position. We observe that varying the offset value from a typical catenary shape to fully taut, the pretension of the mooring line also increases. The experimental measures in each configuration are also included (offset = 25 m), and the largest difference from the numerical predictions is approximately 0.21%. Before starting the fairlead oscillations according to the test matrix, a static test was performed to ensure the accuracy and repeatability of these values.

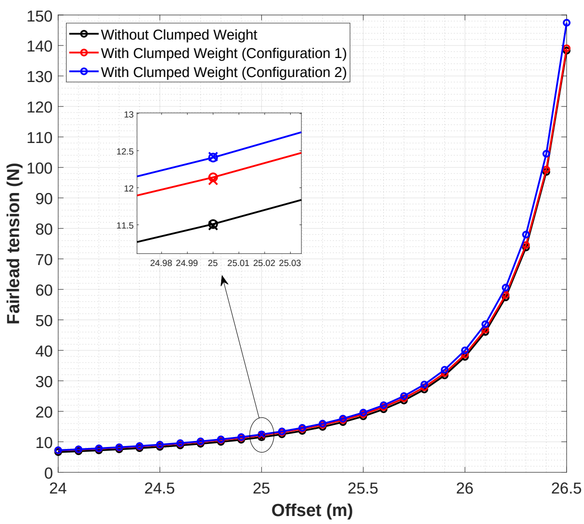

Figure 11. Variation of the tension with offset distance in all configurations. Experimental values are added to the figure with crossed symbols 'x' in the detailed view.

For the selected offset in the experiments (offset $= 25$ m), the maximum difference in the initial pretension is obtained when the clumped weight is placed in Configuration 2, resulting an increment of 10% with respect to the mooring line without clumped weight.

5.1. Mooring Line Dynamics

The fairlead tension measured by the load cell is represented and compared to the fairlead displacement for different values of the period $T = 2.8,\ 3.5,\ 5.5$ s and amplitudes $A = 0.125,\ 0.175,\ 0.225$ m in Figure 12. After reaching a periodic regime and assuming that the measurements satisfy the ergodic theorem, the tension values are the time average during 20 periods and the vertical bars represent its standard deviation.

As can be observed, the maximum and minimum values of the fairlead tension during the cycle are obtained for the minimum displacement with respect to the initial position. As expected, we observe that for constant amplitudes, smaller periods imply larger accelerations and tensions. Similarly, for constant periods, larger amplitudes also imply larger accelerations and fairlead tensions. We clearly observe that the effect of adding a clumped weight in the first configuration (Configuration 1) to the isolated mooring is to increase the fairlead tension for all amplitudes and periods.

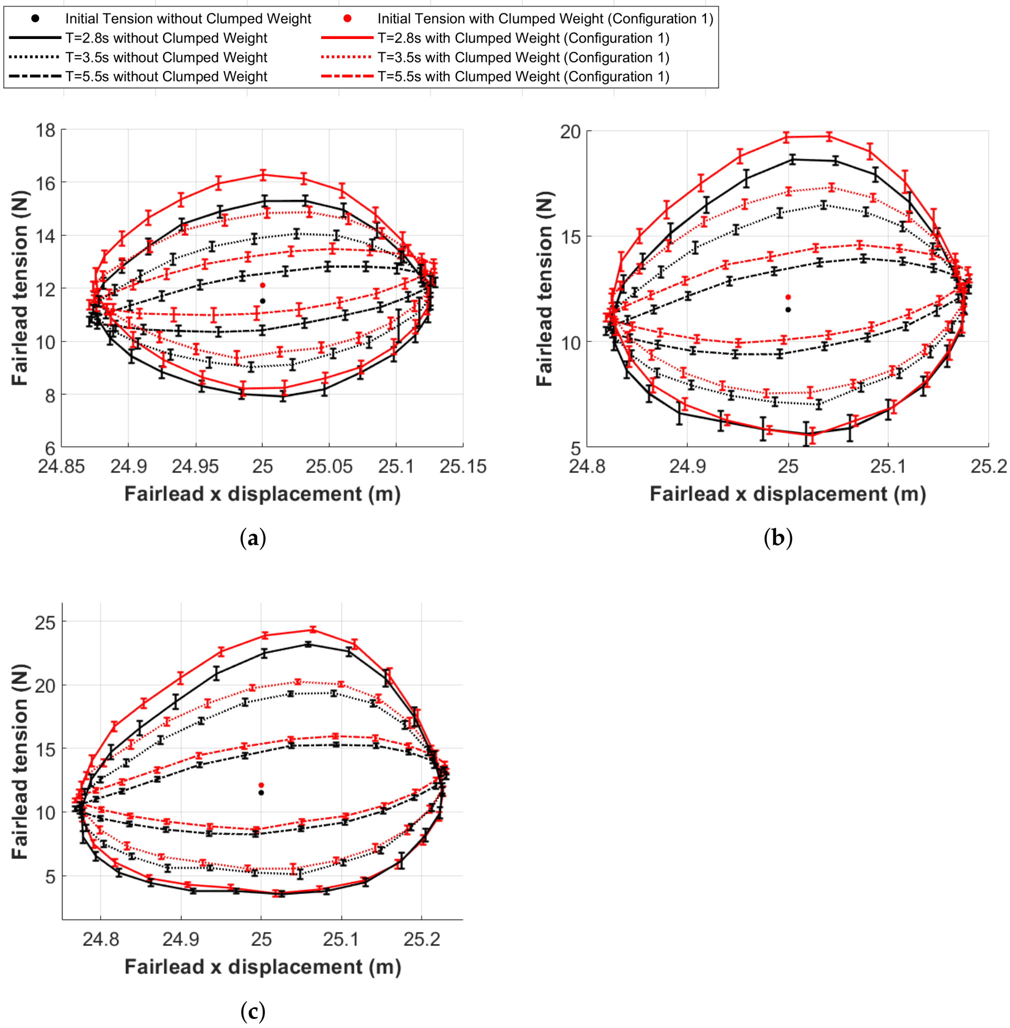

Figure 12. Fairlead tension during the fairlead displacement with and without clumped weight for three different fairlead amplitude values and Configuration 1. (**a**) $A = 0.125$ m. (**b**) $A = 0.175$ m. (**c**) $A = 0.225$ m.

Similarly, in Figure 13, the fairlead tension for the isolated mooring is also compared to the clumped weight (Configuration 2) for the same set of amplitudes and periods. We can observe that the change of the clumped weight position has an important influence on the magnitude of the increase of the fairlead tension. The maximum fairlead tension grows approximately in the same magnitude of the clumped weight in Configuration 1, while the maximum fairlead tension is increased by almost double of this weight in Configuration 2. In other words, when clumped weights are present, the maximum fairlead tension is increased by just 6% in Configuration 1 and by 9% in Configuration 2, with respect to the isolated mooring line.

Additionally, the maximum and minimum fairlead tension of the complete test matrix cases is shown in Tables 8 and 9.

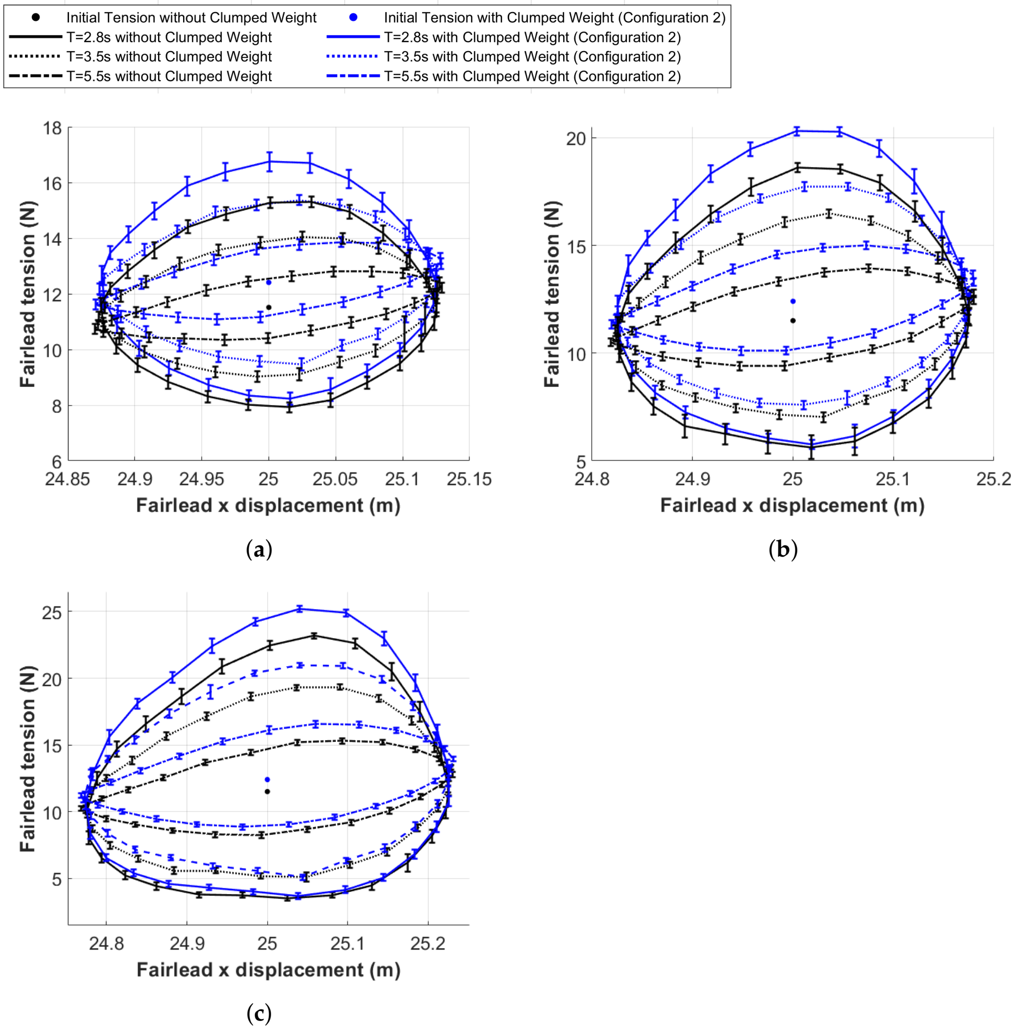

Figure 13. Fairlead tension during the fairlead displacement with and without clumped weight for three different fairlead amplitude values and Configuration 2. (**a**) $A = 0.125$ m. (**b**) $A = 0.175$ m. (**c**) $A = 0.225$ m.

Table 8. Maximum fairlead tension in *N* for all the test matrix and configurations. Notation *WO CW*, *CW1*, and *CW2* denotes mooring line without clumped weight, mooring line with clumped weight (Configuration 1) and mooring line with clumped weight (Configuration 2), respectively.

		Periods (s)							
		2.8	**3.0**	**3.5**	**4.0**	**4.5**	**5.0**	**5.5**	
Amplitudes (m)	**0.125**	15.35	14.88	14.07	13.55	13.2	12.96	12.80	**WO CW**
		16.30	15.78	14.99	14.31	13.92	13.65	13.47	**CW1**
		16.83	16.31	15.37	14.77	14.35	14.06	13.87	**CW2**
	0.150	16.94	16.32	15.19	14.45	13.93	13.57	13.32	**WO CW**
		18.23	17.32	16.07	15.22	14.67	14.40	14.00	**CW1**
		18.44	17.74	16.56	15.71	15.13	15.72	14.42	**CW2**
	0.175	18.68	17.84	16.40	15.66	14.71	14.24	13.89	**WO CW**
		19.86	18.93	17.29	16.18	15.44	14.92	14.54	**CW1**
		20.41	19.50	17.83	16.72	15.94	15.41	15.00	**CW2**
	0.200	20.73	19.68	17.80	16.50	15.63	15.00	14.55	**WO CW**
		21.88	20.74	18.72	17.31	16.35	15.69	15.20	**CW1**
		22.37	21.33	19.60	18.12	17.10	16.28	15.78	**CW2**
	0.225	23.20	21.87	19.46	17.86	16.72	15.95	15.33	**WO CW**
		24.31	22.83	20.35	18.59	17.44	16.58	15.95	**CW1**
		25.24	23.96	21.11	19.38	18.36	17.33	17.05	**CW2**
									Configurations

Table 9. Minimum fairlead tension in *N* for all the test matrix and configurations. Notation *WO CW*, *CW1*, and *CW2* denotes mooring line without clumped weight, mooring line with clumped weight (Configuration 1) and mooring line with clumped weight (Configuration 2), respectively.

		Periods (s)							
		2.8	**3.0**	**3.5**	**4.0**	**4.5**	**5.0**	**5.5**	
Amplitudes (m)	**0.125**	7.826	8.189	8.959	9.558	9.876	10.14	10.34	**WO CW**
		7.758	8.247	9.453	10.04	10.44	10.64	10.90	**CW1**
		8.151	8.626	9.561	10.18	10.59	10.88	11.09	**CW2**
	0.150	6.601	7.116	8.057	8.693	9.289	9.662	9.917	**WO CW**
		6.305	7.064	8.282	9.283	9.832	10.21	10.50	**CW1**
		6.941	7.413	8.55	9.359	9.874	10.33	10.63	**CW2**
	0.175	5.48	5.935	6.999	7.931	8.571	9.04	9.379	**WO CW**
		5.56	6.147	7.036	8.004	8.914	9.578	9.995	**CW1**
		5.797	6.311	7.486	8.419	9.10	9.507	10.07	**CW2**
	0.200	4.388	4.921	6.074	6.895	7.779	8.358	8.805	**WO CW**
		4.626	5.181	6.384	7.163	7.961	8.923	9.402	**CW1**
		4.79	5.40	6.424	7.467	8.297	8.911	9.39	**CW2**
	0.225	3.463	3.93	5.115	6.116	6.912	7.655	8.194	**WO CW**
		3.38	4.222	5.478	6.496	7.326	7.881	8.586	**CW1**
		3.857	4.203	5.449	6.519	7.452	8.117	8.608	**CW2**
									Configurations

A fast Fourier transform (fft) was performed to obtain the power spectra for the mooring line under the imposed motions. The power spectra of the fairlead tension have been analyzed for the complete test matrix. As the fft does not change significantly in our test matrix, a single representative case is presented in Figure 14 for an amplitude of $A = 0.175$ m and $T = 3.5$ s. The 0 Hz frequency value corresponds to the quasi-static case as mentioned in [41]. In all cases, they are mostly dominated by the first harmonic followed by the third and second harmonics. As Figure 14 shows, the presence of the clumped weight along the line does not significantly change the analysis: the power amplitude and frequency of the dominant harmonics being almost the same in all configurations.

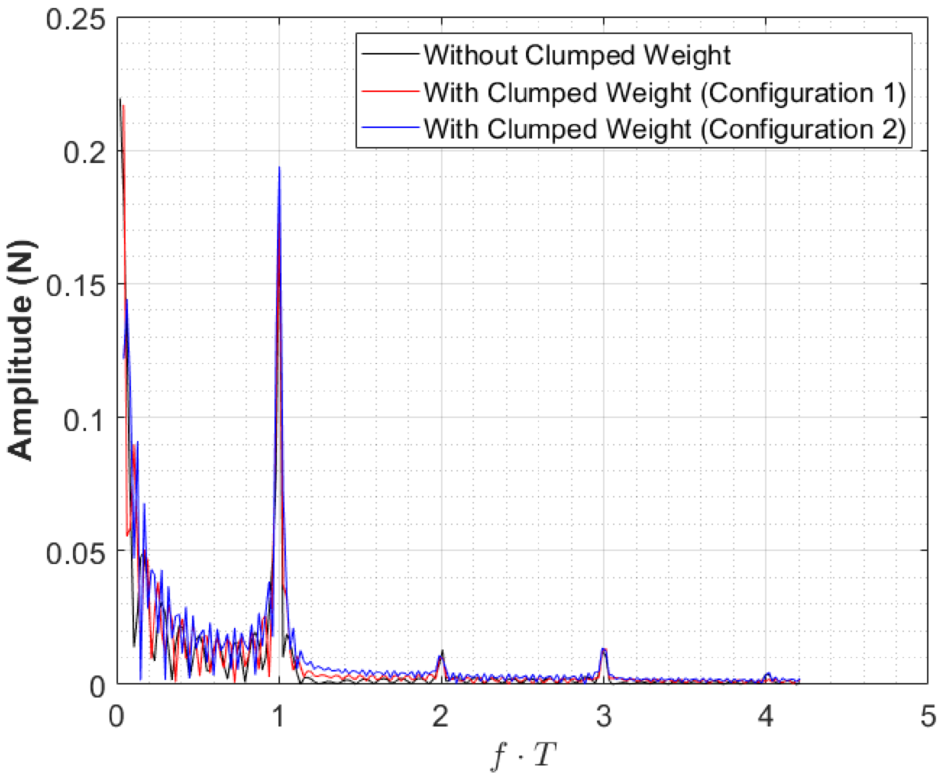

Figure 14. Spectrum plot of the top-end tensions for an amplitude of $A = 0.175$ s and period $T = 3.5$ s for the three tested configurations.

The energy dissipation is computed using the diagram method detailed in [28], where the dissipated energy of the mooring line is the area enclosed in one cycle by the hysteresis loop:

$$E = \oint F_d \cdot d\delta, \tag{29}$$

where F_d and δ are the damping force and the fairlead displacement, respectively.

The dissipation of energy in a mooring line is mainly caused by structural damping, drag with possible VIV, and friction with the seabed [42]. In this study, a simplification is made and the structural damping and friction with the seabed are considered negligible with respect to drag and are modeled as:

$$F_d = F_D = \frac{1}{2}\rho_0 C_D D L_s \dot{\delta}^2 \tag{30}$$

Since the displacement is periodic, $\delta = A \cdot sin(\omega t)$, the dissipation energy can be calculated as:

$$E = 4\int_0^{\delta_{max}} F_d \cdot d\delta = \frac{4}{3}\rho_0 D L C_D A^3 \omega^2 \tag{31}$$

The dissipated energy depends on several factors, such as the frequency and amplitude, as shown in Figures 12 and 13 where the enclosed areas are larger when the frequencies and amplitudes are increased.

The dissipated energy of the complete test matrix computed in dimensional and non-dimensional forms according to Equation (29) are shown in Figure 15. The non-dimensional dissipated energy is obtained by dividing by a reference potential energy, $A \cdot w \cdot H$, as performed by [28]. Both the dimensional dissipated energy and the non-dimensional version present the same tendency, see Figure 15. It can be appreciated that larger amplitudes implicate larger dissipated energy. This pattern is presented in several publications dealing with isolated mooring lines, e.g., [7,23,27]. In the same way, smaller periods increase the dissipated energy. In addition, when clumped weights are present, the pattern is consistent and the damping in all imposed motions is higher, regardless of the location along the line.

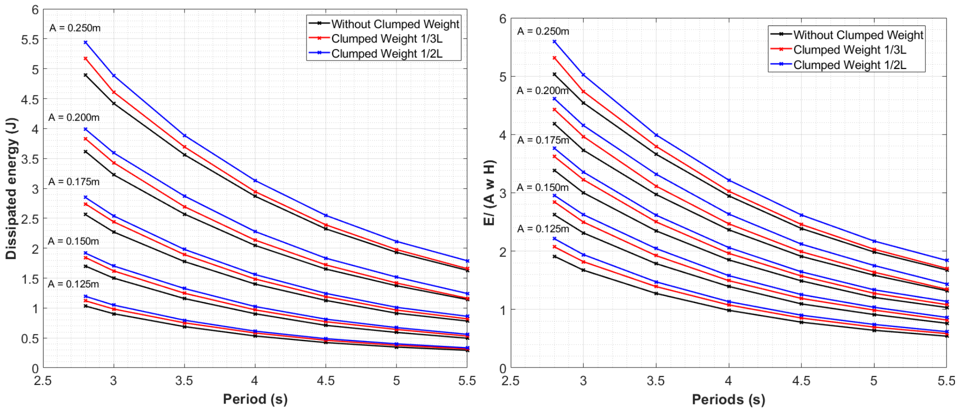

Figure 15. Dissipated energy for all the test matrix. Dimensional form (**left**) and non-dimensional form (**right**).

The dissipated energy for the line without clumped weight is plotted against $\omega^2 A^3$ in Figure 16 for all the motions of the test matrix. Similarly to [23], a good linear fit is accomplished for the experimental results. The same linear tendency is also observed when clumped weights are added in both configurations.

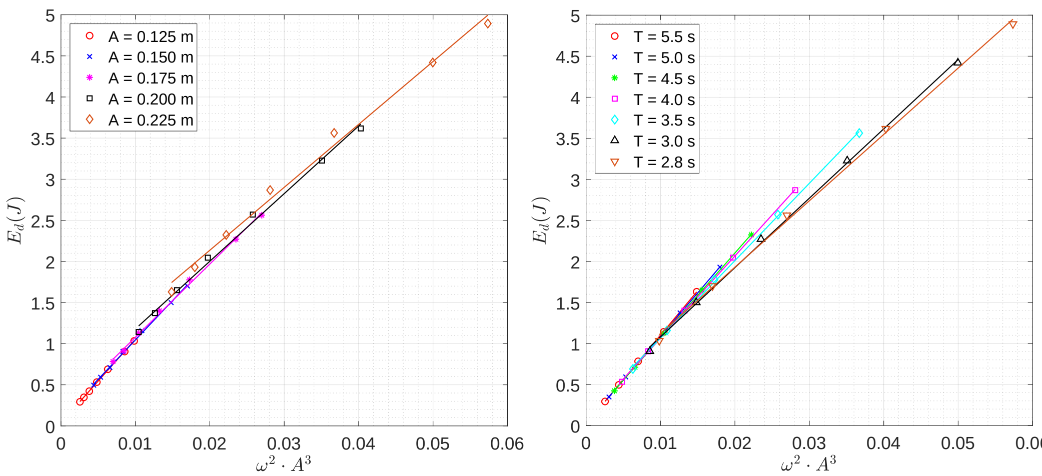

Figure 16. Dissipated energy under the imposed top-end motions for the mooring line without clumped weight.

Assuming that the drag coefficient C_D can be obtained from the slope of the fitted curves, which is $\frac{4}{3}\rho_0 DLC_D$, the mean value obtained for the complete test matrix was $C_D = 1.75$ for the isolated mooring line, which is a little higher than the standard value used for the simulations $C_{Dn} = 1.455$, see Section 4.4. The mean values of C_D obtained when clumped weights are present were 1.82 and 1.90 for Configuration 1 and Configuration 2, respectively. This increase of the damping coefficient explains why the line dissipates more energy when clumped weights are added.

The non-dimensional increase of dissipated energy due to the clumped weight is expressed by Equation (32).

$$\frac{\Delta E}{E_{CW}} = \frac{\Delta E}{\rho_0 A^3 \omega^2 D_{CW}^2} \tag{32}$$

The dimensionless increase of dissipated energy for both clump weight configurations with respect to the line without clump weight, for each of the different amplitudes and periods tested, is shown in Figure 17. The amplitude of the motion has more influence than the period in the increase of dissipated energy, as seen in Figure 17. Configuration 2 has an evident increase of the dissipated energy, almost two times higher than Configuration 1 for all cases. The presence of the clumped weights shows a more dominant effect for smaller amplitudes in terms of dissipated energy.

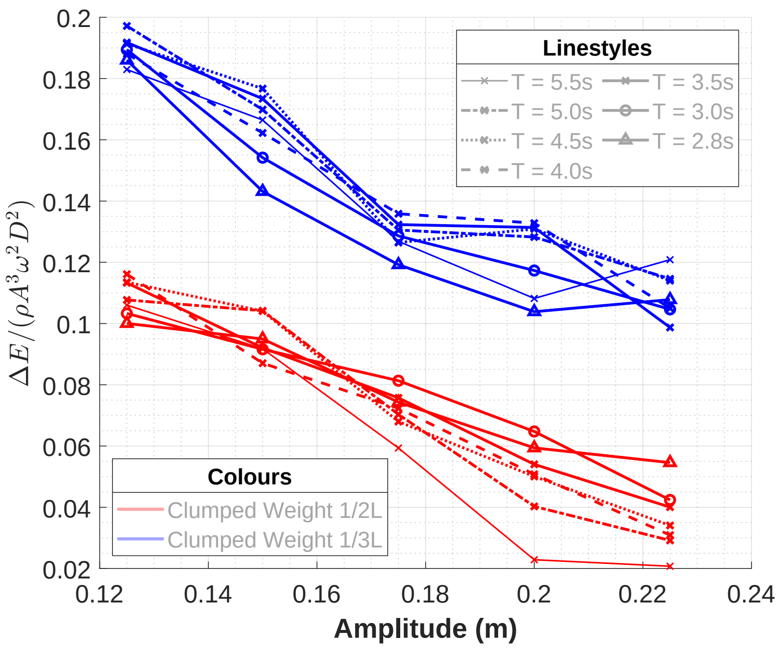

Figure 17. Dimensionless increase of dissipated energy due to the Clumped weights.

5.2. Mooring Line Kinematics

In this subsection, the results of the image processing of the camera recordings will be presented. The postprocessing of the visual data was performed with MATLAB tools and consisted of applying a moving method for detecting local outliers according to a specified window. A Piecewise Cubic Hermite Interpolating Polynomial has been used for replacing the outliers. Finally, a classical filter for frequencies higher than the third harmonic has been applied and optical errors have been excluded.

Figure 18 shows the trajectories of markers 2 to 10 for the mooring line without clumped weight and with clumped weight (Configuration 1). The results show the same pattern described in previous publications [7,10], where the points near the top of the line move very similarly to the fairlead, while deeper points move more vertically. Despite the slightly changed trajectories of the points, the pattern barely changes with the addition of clumped weights in both configurations. Trajectories of the mooring line with clumped weight (Configuration 2) has not been added because the similarity in the results overlaps with the other two configurations with a slight change of the position because of the different shape of the catenary.

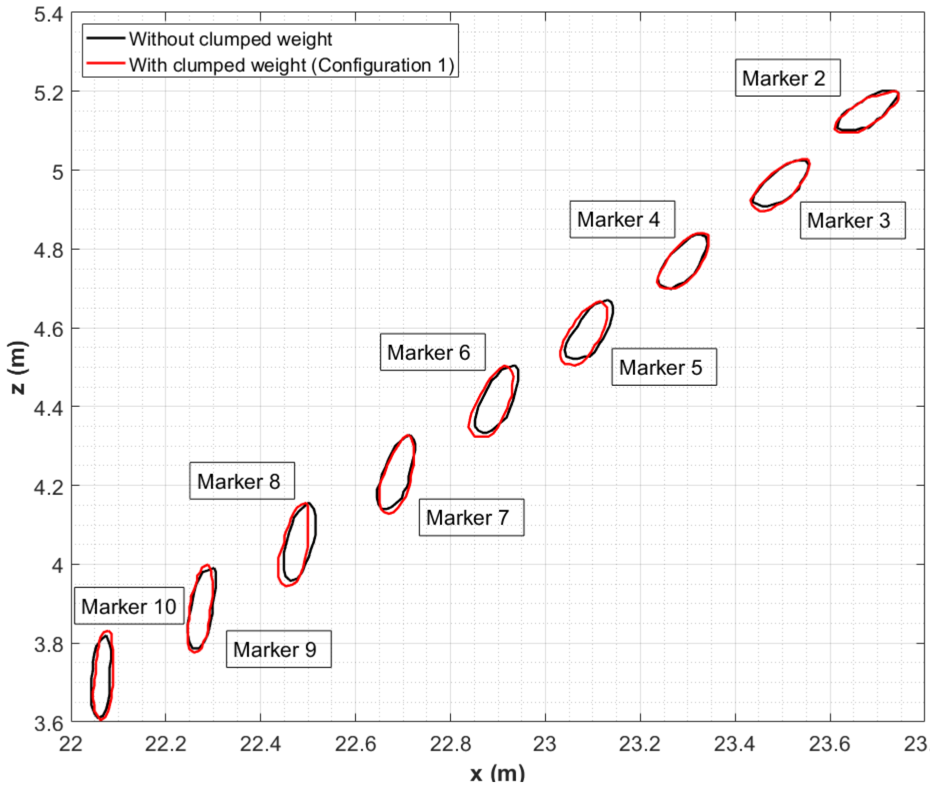

Figure 18. Trajectories of the tracked points of the mooring line for a top-end motion of an Amplitude of 0.175 m and periods 3.5 s. Markers 2 to 10 are indicated in the figure.

Figure 19 presents the tracked motions of three mooring line points with and without clumped weight in Configuration 1, for an amplitude of 0.125 m and three periods of $2.8, 3.5, 5.5$ s. For all points, the ranges of motion in the x- and z-directions of the reference system in Figure 9 are practically the same, with some changes observed for the shortest periods, and a slight change in the initial position of the marker due to the different catenary curves caused by the presence of the clumped weight.

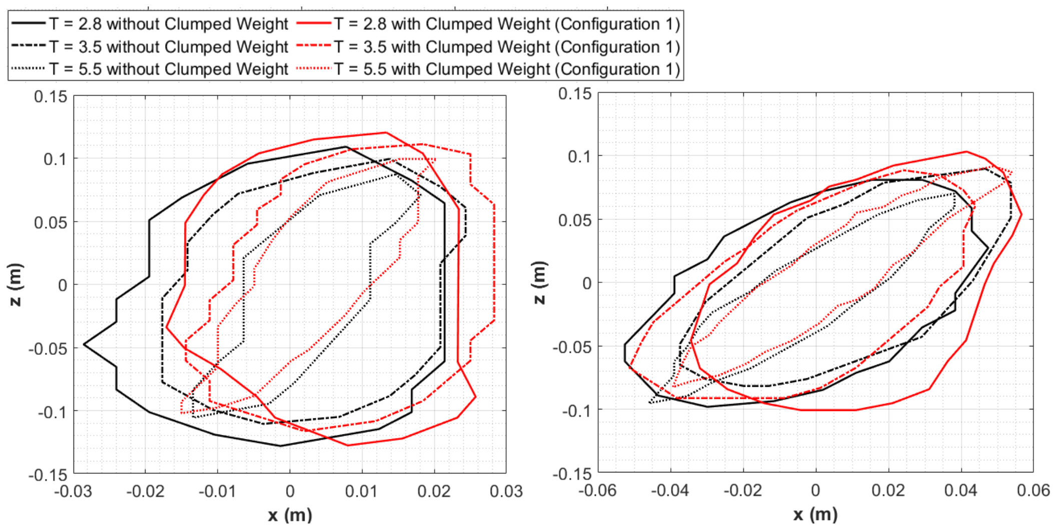

(**a**) (**b**)

Figure 19. *Cont.*

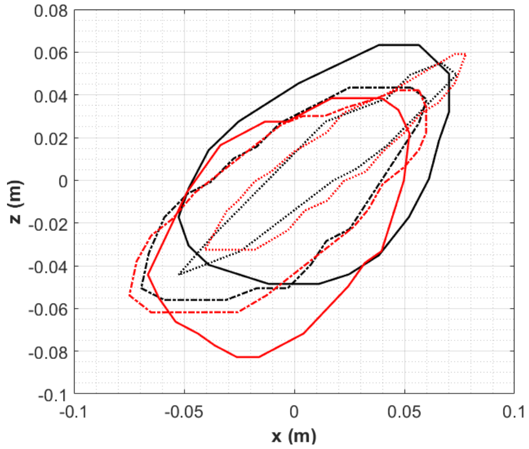

(**c**)

Figure 19. Tracked motions of three points of the mooring line, for a top-end motion of an Amplitude of 0.125 m and periods 2.8, 3.5, 5.5 s. (**a**) Trajectories of the mooring line lower point of Figure 18 (Marker 9). (**b**) Trajectories of the mooring line middle point of Figure 18 (Marker 5). (**c**) Trajectories of the mooring line upper point of Figure 18 (Marker 2).

6. Numerical Results

The numerical code OPASS has been validated with these new experimental results, where clumped weights are part of the mooring line. First, the fairlead tension in the absence of clumped weights has been computed and compared with the experimental results for three oscillation periods $T = 2.8,\ 3.5,\ 5.5$ s and two amplitudes $A = 0.125,\ 0.225$ m in Figure 20, and for two oscillations periods $T = 2.8,\ 5.5$ s and five amplitudes values $A = 0.225,\ 0.220,\ 0.175,\ 0.150, 0.125$ m in Figure 21. As can be observed, the prediction of the numerical tool approximates the values measured in the experiments for all periods and amplitudes tested very well. When the clumped weight is added in both configurations, the prediction of the numerical code is still valid, see Figures 22 and 23 for Configuration 1 and Figures 24 and 25 for Configuration 2. From these figures, a slightly overpredicted fairlead tension at the maximum tension condition can be observed. This tendency appears in all the cases tested. In addition, the numerical code can capture the increase of the fairlead tension in approximately the same proportion as the experimental results shown in Figures 12 and 13.

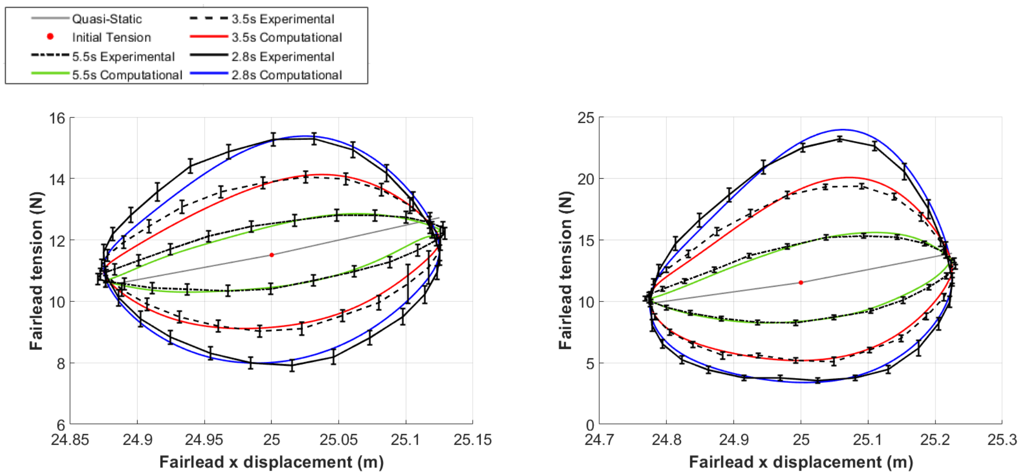

(**a**) (**b**)

Figure 20. Comparison between the computed fairlead tension values and the experimental measurements of the isolated mooring line for two different oscillation amplitudes $A = 0.125,\ 0.225$ m and three different periods $T = 2.8,\ 3.5,\ 5.5$ s for the isolated mooring line. (**a**) $A = 0.125$ m. (**b**) $A = 0.225$ m.

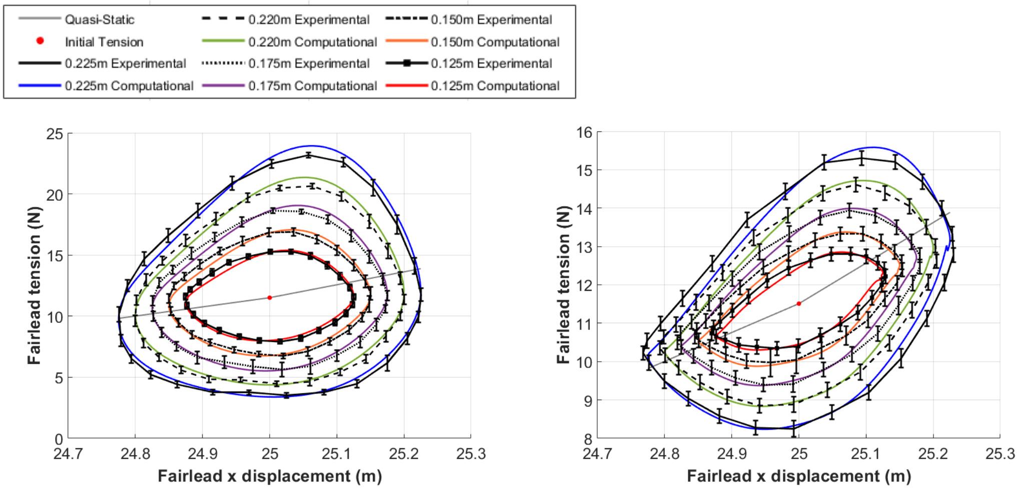

(**a**) (**b**)

Figure 21. Comparison between the computed fairlead tension values and the experimental measurements of the isolated mooring line for two different oscillation amplitudes $A = 0.225, 0.220, 0.175, 0.150, 0.125$ m and two different periods $T = 2.8,\ 5.5$ s for the isolated mooring line. (**a**) $T = 2.8$ s. (**b**) $T = 5.5$ s.

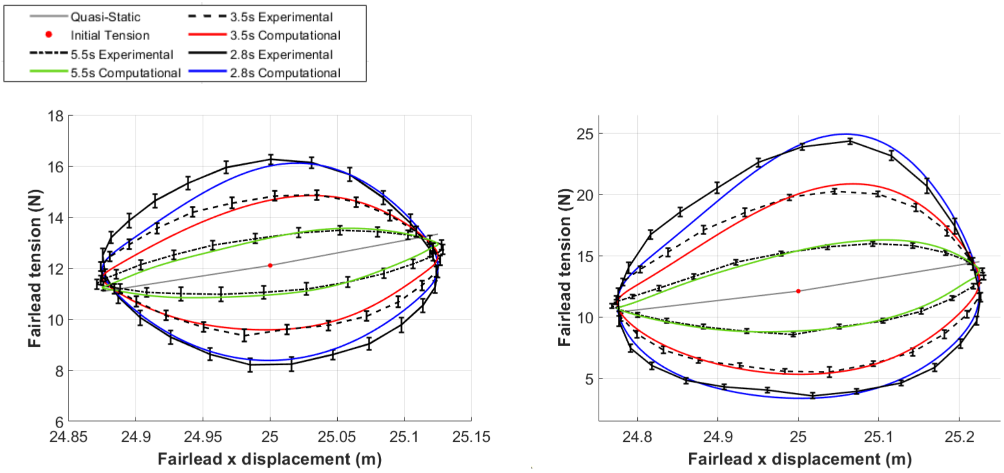

(**a**) (**b**)

Figure 22. Comparison between the computed fairlead tension values and the experimental measurements of the mooring line with the clumped weight in configuration 1 for two different oscillation amplitudes $A = 0.125,\ 0.225$ m and three different periods $T = 2.8,\ 3.5,\ 5.5$ s for the isolated mooring line. (**a**) $A = 0.125$ m. (**b**) $A = 0.225$ m.

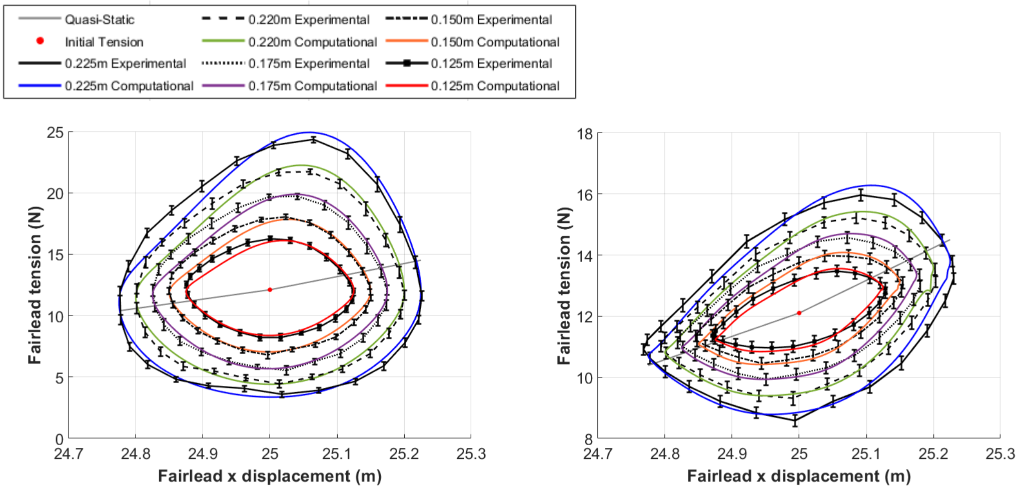

Figure 23. Comparison between the computed fairlead tension values and the experimental measurements with clumped weight in configuration 1 for different oscillation amplitudes $A = 0.225$, 0.220, 0.175, 0.150, 0.125 m and two different periods $T = 2.8,\ 5.5$ s for the isolated mooring line. (**a**) $T = 2.8$ s. (**b**) $T = 5.5$ s.

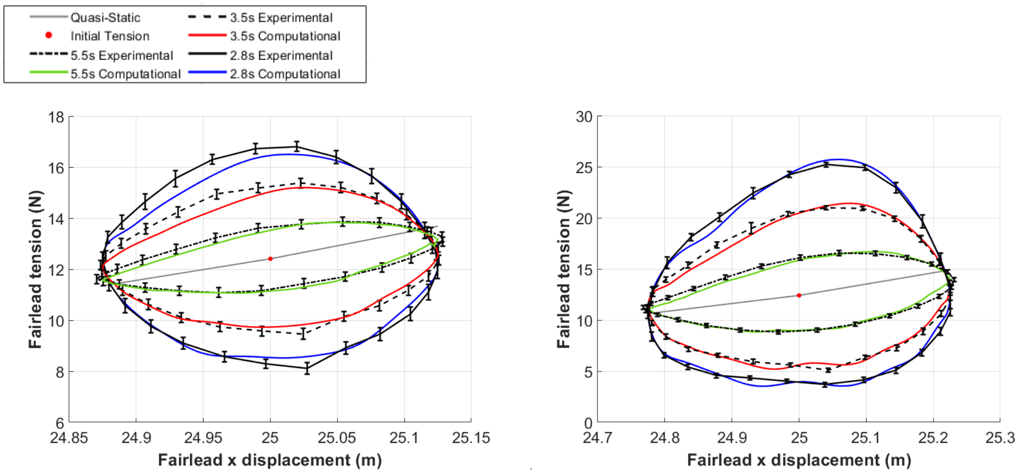

Figure 24. Comparison between the computed fairlead tension values and the experimental measurements of the mooring line with the clumped weight in configuration 2 for two different oscillation amplitudes $A = 0.125,\ 0.225$ m and three different periods $T = 2.8,\ 3.5,\ 5.5$ s for the isolated mooring line. (**a**) $A = 0.125$ m. (**b**) $A = 0.225$ m.

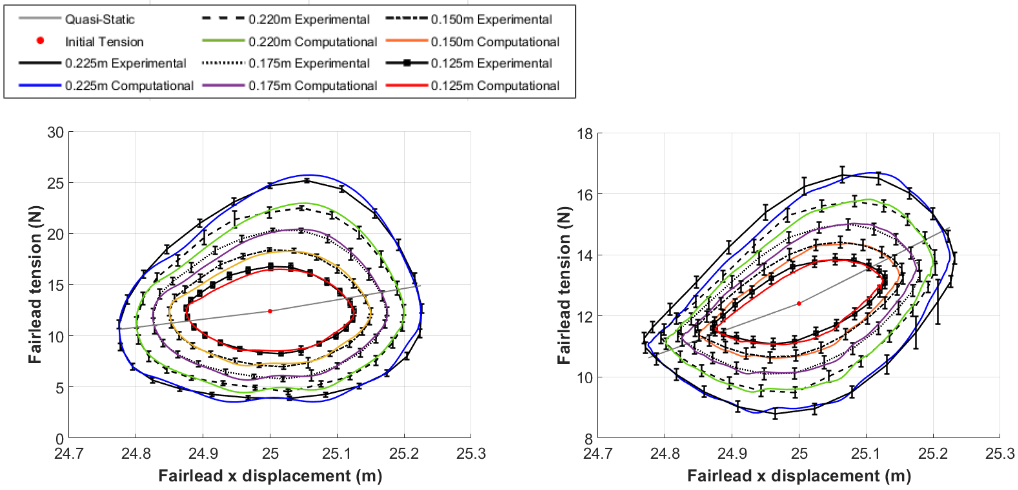

(**a**) (**b**)

Figure 25. Comparison between the computed fairlead tension values and the experimental measurements with clumped weight in configuration 2 for different oscillation amplitudes $A = 0.225$, 0.220, 0.175, 0.150, 0.125 m and two different periods $T = 2.8,\ 5.5$ s for the isolated mooring line. (**a**) $T = 2.8$ s. (**b**) $T = 5.5$ s.

The trajectory of part of the mooring line in the absence of clumped weights has been computed numerically for three oscillation periods $T = 2.8,\ 3.5,\ 5.5$ s and one amplitude $A = 0.125$ m, see Figure 26. It can be observed that the prediction of the numerical tool approximates the values measured in the experiments for all periods and amplitudes tested very well. When the clumped weight is added, the prediction of the numerical code is still valid, see, for example, Figure 27 for Configuration 1.

The optical errors have not been corrected in the postprocessing and their effects are present for the nodes placed at the ends: markers 1 to 3 and 8 to 11. This could be the explanation for why the trajectories numerically obtained have better agreement with the experimental results for the central nodes (Markers 4 to 7). This could be improved in the near future using several cameras instead of only a single one.

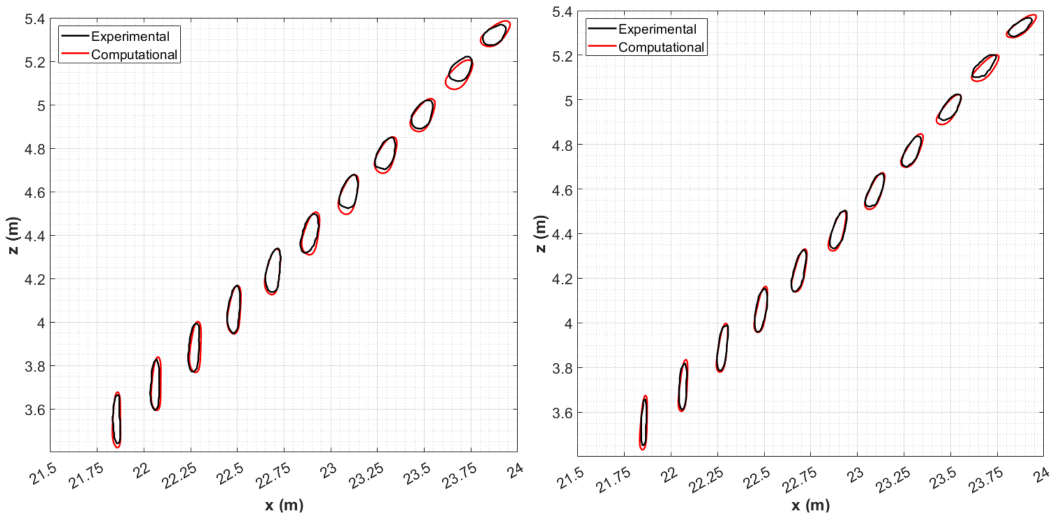

(**a**) (**b**)

Figure 26. *Cont.*

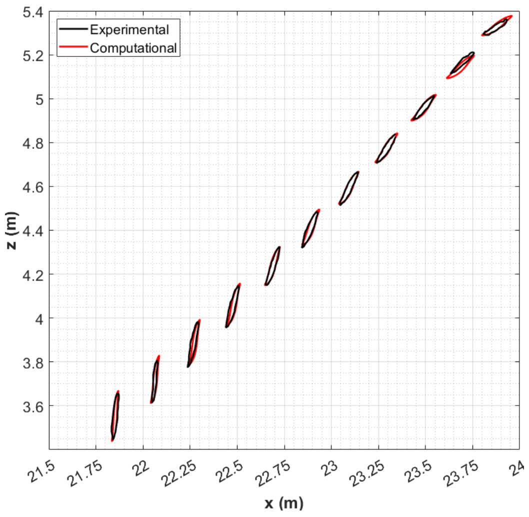

(**c**)

Figure 26. Comparison between computed trajectories of catenary nodes and experimental tracked points for different oscillation periods $T = 2.8,\ 3.5,\ 5.5$ s and amplitude $A = 0.125$ m for the isolated mooring line without clumped weight. (**a**) $T = 2.8$ s. (**b**) $T = 3.5$ s. (**c**) $T = 5.5$ s.

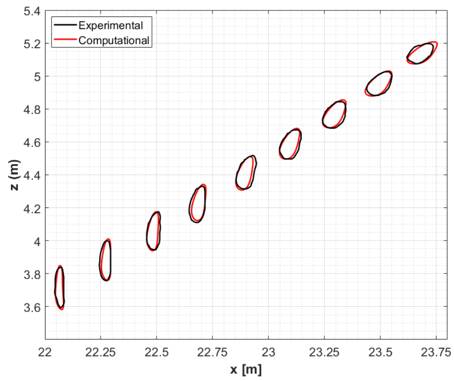

(**a**)

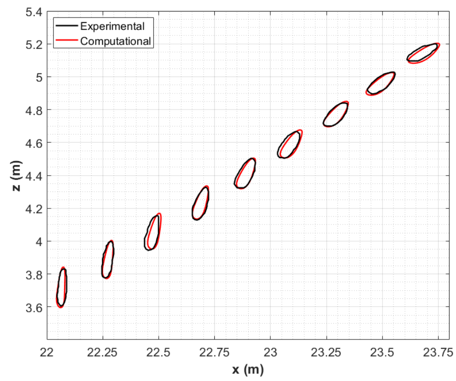

(**b**)

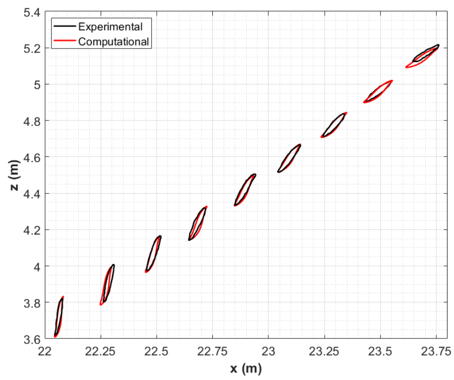

(**c**)

Figure 27. Comparison between computed trajectories of catenary nodes and experimental tracked points for different oscillation periods $T = 2.8,\ 3.5,\ 5.5$ s and amplitude $A = 0.125$ m for the isolated mooring line with clumped weight (Configuration 1). (**a**) $T = 2.8$ s. (**b**) $T = 3.5$ s. (**c**) $T = 5.5$ s.

7. Conclusions

The influence of the clumped weights when added to mooring line dynamics is studied from a dual point of view: experimentally, using scaled experiments in a towing tank, and numerically, using a finite element numerical tool where the action of the clumped weights has been modeled. The performance of the numerical tool is notably accurate when its predictions are compared to the experiments for both an isolated line and for the presence of clumped weights, in terms of fairlead tension and line kinematics.

The first evidence observed is that the geometric stiffness of the mooring line in the horizontal plane was increased when a clumped weight was added. Consequently, the disadvantage of this addition is that more rigid systems are more loaded and therefore require more expensive lines with larger breaking loads. The advantage of the stiffness increment obtained with the addition of the clumped weights is that the fairlead tension is increased for the same excursion, and therefore, we should expect a surge motion reduction of the moored platform in practical applications.

As expected, the experimental results show an increase in the fairlead tension when clumped weights are present, approximately increasing its value by the weight of the clumped weight in absolute terms and, in relative terms, increasing it between 6% and 9% of the maximum fairlead tension with respect to the isolated mooring line.

When the clumped weight is closer to the fairlead, the line dissipates less energy than when it is placed further away. Therefore, setting the clumped weight farther from the fairlead with the obvious limitation of seabed contact seems to be an adequate practice to reduce the surge motion of the moored platform. Keeping in mind that the role of the clumped weights is also to increase the dissipated energy, the clumped weight's presence is more effective in terms of non-dimensional energy dissipation when low amplitude motions of the fairlead are present.

To track the mooring line kinematics, a low cost system based on an image processing code and submerged cameras has been developed to search and locate the mooring line movements. Good agreement between the trajectories obtained after the image postprocessing and numerical counterparts is shown for the central nodes tracked, while the nodes placed at the ends seem to be affected by optical errors.

Previously validated for an isolated line OPASS code, a simulation tool specifically designed for mooring line dynamics now includes the possibility of clumped weight implementation and has been validated against experiments for two different clumped weight configurations with good accuracy. However, when the fairlead accelerations grow, and the mooring line excitation is more violent, the numerical approach tends to overpredict the maximum tension in the fairlead. This could be due to the difficulty of accurately determining the line drag and added mass coefficients.

Author Contributions: T.L.-O.: conceptualization, investigation, software, formal analysis, data curation, writing—original draft, writing—review and editing; L.M.G.-G.: conceptualization, methodology, investigation, writing—original draft, and writing—review and editing; J.C.-S.: writing—review and editing; A.M.L.: investigation, experimental setup, experiments; L.S.Y.: investigation, experimental setup, experiments, and data curation; A.B.B.: investigation, experimental setup, experiments; N.V.V.: experiments. All authors have read and agreed to the published version of the manuscript.

Funding: This research was founded by the Spanish Ministry of Economy and Competitiveness (MEC) under grant RTI2018-096791-B-C21 and RTI2018-096791-B-C22 *Hidrodinámica de elementos de amortiguamiento del movimiento de aerogeneradores flotantes*.

Institutional Review Board Statement: Not applicable.

Informed Consent Statement: Not applicable.

Acknowledgments: All the authors would like to thank to Jon Martinez for his help in the development of the Matlab script for tracking motion of the mooring line. The authors would like to thank Ciaran Stone for his valuable assistance during the preparation of this manuscript.

Conflicts of Interest: All authors have participated in the conception, analysis, and interpretation of the data, revising the article critically and approving the final version. The authors have no affiliation with any organization with a direct or indirect financial interest in the subject matter discussed in the manuscript. The authors confirm that this work is original and has not been published elsewhere.

Appendix A

Appendix A.1. Load Cell Uncertainties

As explained in Section 3.2, before performing the experimental campaign, the load cell was calibrated with different weights ranging from 0 to 6 Kg. A fitted curve of the measured data using a linear interpolation $val(x) = 0.08992x - 0.0001097$, and an R^2 of 0.9999 was performed, as represented in Figure A1.

The uncertainties were estimated by adding the standard deviation of the residuals σ to the combined standard uncertainty of the instrument $U_c = 0.001528$ mV/V that takes into account the temperature, deformation, and weight uncertainties.

$$error = \sqrt{\sigma^2 + U_c^2} = \sqrt{(0.000196\ \mathrm{mV/V})^2 + (0.001528\ \mathrm{mV/V})^2} \tag{A1}$$

The error in the measurements was estimated according to Equation (A1), resulting in an error of ± 0.179 N after correcting with the calibration line, represented in Figure A1.

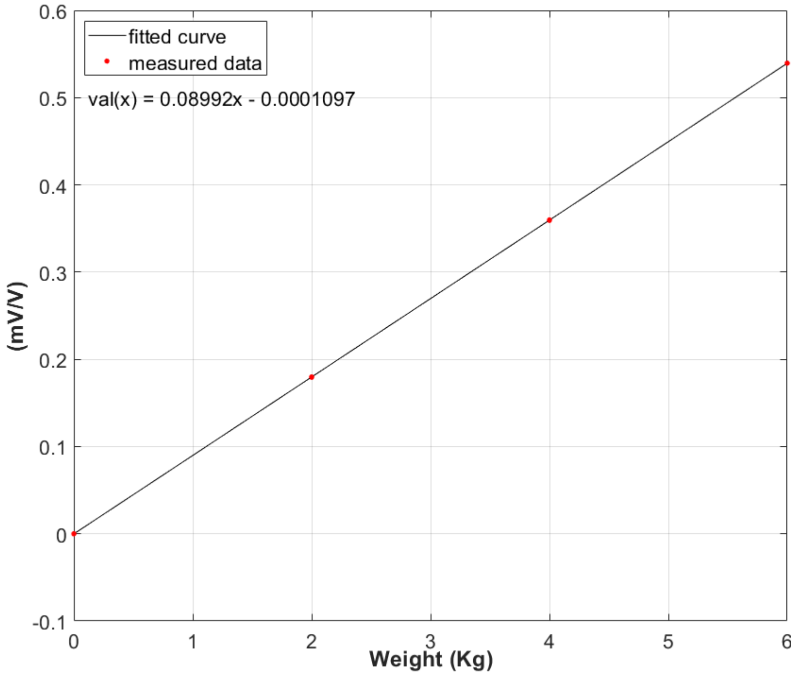

Figure A1. Calibration curve for the one-component load cell.

Appendix A.2. Accelerometer Uncertainties

As explained in Section 3.2, before performing the experimental campaign the accelerometer was calibrated with different accelerations ranging from -9.81 to 9.81 m/s^2 in the x-direction. A fitted curve of the measured data using a linear interpolation $val(x) = -0.09355x + 0.9178$ and an R^2 of 0.9999 was performed, as represented in Figure A2.

The uncertainties were estimated by adding the standard deviation of the residuals σ to the combined standard uncertainty of the instrument $U_c = 0.002153$ mV/V.

$$error = \sqrt{\sigma^2 + U_c^2} = \sqrt{(0.000683\ \mathrm{mV/V})^2 + (0.002153\ \mathrm{mV/V})^2} \tag{A2}$$

The error in the measurements was estimated according to Equation (A2), resulting in an error of ± 0.0131 m/s^2 from the acceleration due to gravity after correcting with the calibration line, represented in Figure A2.

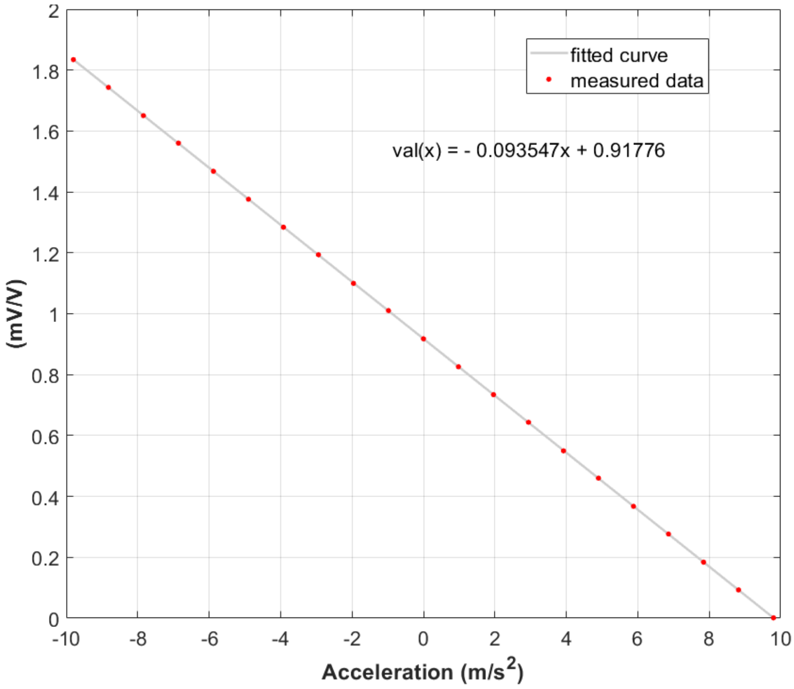

Figure A2. Calibration curve for the three-component accelerometer in the *x*-direction.

References

1. Ramírez, L.; Fraile, D.; Brindley, G. Offshore Wind in Europe—Key Trends and Statistics 2020. 2020. Available online: https://windeurope.org/intelligence-platform/product/offshore-wind-in-europe-key-trends-and-statistics-2020/ (accessed on 8 May 2021).
2. Hsu, W.Y.; Chuang, T.C.; Yang, R.Y.; Hsu, W.T.; Thiagarajan, K.P. An Experimental Study of Mooring Line Damping and Snap Load in Shallow Water. *J. Offshore Mech. Arct. Eng.* **2019**, *141*, 051603. [CrossRef]
3. Davidson, J.; Ringwood, J.V. Mathematical modelling of mooring systems for wave energy converters—A review. *Energies* **2017**, *10*, 666. [CrossRef]
4. Hsu, W.t.; Thiagarajan, K.P.; MacNicoll, M.; Akers, R. Prediction of extreme tensions in mooring lines of a floating offshore wind turbine in a 100-year storm. In *International Conference on Offshore Mechanics and Arctic Engineering*; American Society of Mechanical Engineers: New York, NY, USA, 2015; Volume 56574, p. V009T09A050.
5. Shah, A.; Umar, A.; Siddiqui, N. A methodology for assessing the reliability of taut and slack mooring systems against instability. *Ocean Eng.* **2005**, *32*, 1216–1234. [CrossRef]
6. Luo, Y. Optimum Design Of Clump Weights For Offshore Mooring Systems. In Proceedings of the Second International Offshore and Polar Engineering Conference, San Francisco, CA, USA, 14 June 1992.
7. Barrera, C.; Guanche, R.; Losada, I.J. Experimental modelling of mooring systems for floating marine energy concepts. *Mar. Struct.* **2019**, *63*, 153–180. [CrossRef]
8. Chen, L.; Basu, B. Development of an open-source simulation tool for mooring systems. In Proceedings of the 2018 Civil Engineering Research in Ireland Conference, Dublin, Ireland, 29–30 August 2018; pp. 823–828.
9. Barrera, C.; Guanche, R.; Rodríguez, Á.; Armesto, J.A.; Losada, I.J. On the importance of mooring system parametrisation for accurate floating structure designs. *Mar. Struct.* **2020**, *72*, 102765. [CrossRef]
10. Azcona, J.; Munduate, X.; González, L.; Nygaard, T.A. Experimental validation of a dynamic mooring lines code with tension and motion measurements of a submerged chain. *Ocean Eng.* **2017**, *129*, 415–427. [CrossRef]
11. Crudu, L.; Obreja, D.; Marcu, O. Moored offshore structures-evaluation of forces in elastic mooring lines. In *IOP Conference Series: Materials Science and Engineering*; IOP Publishing: Bristol, UK, 2016; Volume 147, p. 012096.
12. Liu, Z.; Tu, Y.; Wang, W.; Qian, G. Numerical analysis of a catenary mooring system attached by clump masses for improving the wave-resistance ability of a spar buoy-type floating offshore wind turbine. *Appl. Sci.* **2019**, *9*, 1075. [CrossRef]
13. Yuan, Z.M.; Incecik, A.; Ji, C. Numerical study on a hybrid mooring system with clump weights and buoys. *Ocean Eng.* **2014**, *88*, 1–11. [CrossRef]
14. Ji, C.; Yuan, Z. Experimental study of a hybrid mooring system. *J. Mar. Sci. Technol.* **2015**, *20*, 213–225. [CrossRef]
15. Barbanti, G.; Marino, E.; Borri, C. Mooring system optimization for a spar-buoy wind turbine in rough wind and sea conditions. In *Conference of the Italian Association for Wind Engineering*; Springer: Berlin/Heidelberg, Germany, 2018; pp. 87–98.
16. Xu, K.; Larsen, K.; Shao, Y.; Zhang, M.; Gao, Z.; Moan, T. Design and comparative analysis of alternative mooring systems for floating wind turbines in shallow water with emphasis on ultimate limit state design. *Ocean Eng.* **2021**, *219*, 108377. [CrossRef]

17. Sirigu, S.A.; Bonfanti, M.; Begovic, E.; Bertorello, C.; Dafnakis, P.; Giorgi, G.; Bracco, G.; Mattiazzo, G. Experimental investigation of the mooring system of a wave energy converter in operating and extreme wave conditions. *J. Mar. Sci. Eng.* **2020**, *8*, 180. [CrossRef]
18. Hermawan, Y.A.; Furukawa, Y. Coupled three-dimensional dynamics model of multi-component mooring line for motion analysis of floating offshore structure. *Ocean Eng.* **2020**, *200*, 106928. [CrossRef]
19. Bruschi, N.; Ferri, G.; Marino, E.; Borri, C. Influence of Clumps-Weighted Moorings on a Spar Buoy Offshore Wind Turbine. *Energies* **2020**, *13*, 6407. [CrossRef]
20. Cabrerizo-Morales, M.; Molina-Sanchez, R.; Pérez-Rojas, L. Small-Scale Study of Mooring Line Tension Thresholds Based on Impulsive Load Analysis during Big Floating Structure Operation and Commissioning. *Water* **2021**, *13*, 1056. [CrossRef]
21. Nakajima, T.; Motora, S.; Fujino, M. On the dynamic analysis of multi-component mooring lines. In Proceedings of the Offshore Technology Conference, Houston, TX, USA, 3–6 May 1982.
22. Gao, X.; Liu, X.; Xue, X.; Chen, N.Z. Fracture mechanics-based mooring system fatigue analysis for a spar-based floating offshore wind turbine. *Ocean Eng.* **2021**, *223*, 108618. [CrossRef]
23. Li, Y.; Guo, S.; Chen, W.; Yan, D.; Song, J. Analysis on restoring stiffness and its hysteresis behavior of slender catenary mooring-line. *Ocean Eng.* **2020**, *209*, 107521. [CrossRef]
24. Qiao, D.; Yan, J.; Liang, H.; Ning, D.; Li, B.; Ou, J. Analysis on snap load characteristics of mooring line in slack-taut process. *Ocean Eng.* **2020**, *196*, 106807. [CrossRef]
25. Bergdahl, L.; Palm, J.; Eskilsson, C.; Lindahl, J. Dynamically scaled model experiment of a mooring cable. *J. Mar. Sci. Eng.* **2016**, *4*, 5. [CrossRef]
26. Huse, E. Influence of mooring line damping upon rig motions. In Proceedings of the Offshore Technology Conference, Houston, TX, USA, 5–8 May 1986.
27. Yan, J.; Qiao, D.; Li, B.; Wang, B.; Liang, H.; Ning, D.; Ou, J. An improved method of mooring damping estimation considering mooring line segments contribution. *Ocean Eng.* **2021**, *239*, 109887. [CrossRef]
28. Webster, W.C. Mooring-induced damping. *Ocean Eng.* **1995**, *22*, 571–591. [CrossRef]
29. Huse, E.; Matsumoto, K. Practical estimation of mooring line damping. In Proceedings of the Offshore Technology Conference, Houston, TX, USA, 2–5 May 1988.
30. Kitney, N.; Brown, D.T. Experimental investigation of mooring line loading using large and small-scale models. *J. Offshore Mech. Arct. Eng.* **2001**, *123*, 1–9. [CrossRef]
31. Hall, M. MoorDyn V2: New Capabilities in Mooring System Components and Load Cases. In *International Conference on Offshore Mechanics and Arctic Engineering*; American Society of Mechanical Engineers: New York, NY, USA, 2020; Volume 84416, p. V009T09A078.
32. Roddier, D.; Cermelli, C.; Aubault, A.; Weinstein, A. WindFloat: A floating foundation for offshore wind turbines. *J. Renew. Sustain. Energy* **2010**, *2*, 033104. [CrossRef]
33. Robertson, A.; Jonkman, J.; Masciola, M.; Song, H.; Goupee, A.; Coulling, A.; Luan, C. *Definition of the Semisubmersible Floating System for Phase II of OC4*; Technical Report; National Renewable Energy Lab. (NREL): Golden, CO, USA, 2014.
34. Jonkman, J.M. *Dynamics Modeling and Loads Analysis of an Offshore Floating Wind Turbine*; University of Colorado at Boulder: Boulder, NT, USA, 2007.
35. Morison, J.; Johnson, J.; Schaaf, S. The force exerted by surface waves on piles. *J. Pet. Technol.* **1950**, *2*, 149–154. [CrossRef]
36. White, F.M. *Fluid Mechanics*; Tata McGraw-Hill Education: New York, NY, USA, 1979.
37. Patton, K.T. *An Experimental Determination of Hydrodynamic Masses and Mechanical Impedances*; Technical Report; Navy Underwater Sound Lab.: New London, CT, USA, 1965.
38. OrcaFlex, M. *Version 9.8 b*; Orcina Ltd.: Daltongate, LA, USA, 2014.
39. Veritas, B. NR 493 R02 E. *Classif. Mooring Syst. Perm. Offshore Units* **2002**, *583*.
40. Veritas, D.N. *Offshore Standard DNV-OS-E301 Position Mooring*; Det Norske Veritas: Høvik, Norway, 2010.
41. Guo, S.; Chen, W.; Fu, Y. Non-linearly restoring performance of SFT's catenary mooring-lines under consideration of its dynamic behaviors. *Procedia Eng.* **2016**, *166*, 202–211. [CrossRef]
42. Qiao, D.; Ou, J. Mooring line damping estimation for a floating wind turbine. *Sci. World J.* **2014**, *2014*, 840283. [CrossRef]